Accepted for publication in *The Astronomical Journal*
Preprint typeset using LaTeX style emulateapj v. 11/10/09

A MOLECULAR STAR FORMATION LAW IN THE ATOMIC GAS DOMINATED REGIME IN NEARBY GALAXIES

Andreas Schruba[1], Adam K. Leroy[2,11], Fabian Walter[1], Frank Bigiel[3], Elias Brinks[4], W. J. G. de Blok[5], Gaelle Dumas[1], Carsten Kramer[6], Erik Rosolowsky[7], Karin Sandstrom[1], Karl Schuster[8], Antonio Usero[9], Axel Weiss[10], Helmut Wiesemeyer[10]

Accepted for publication in The Astronomical Journal

ABSTRACT

We use the IRAM HERACLES survey to study CO emission from 33 nearby spiral galaxies down to very low intensities. Using 21-cm line atomic hydrogen (H I) data, mostly from THINGS, we predict the local mean CO velocity based on the mean H I velocity. By re–normalizing the CO velocity axis so that zero corresponds to the local mean H I velocity we are able to stack spectra coherently over large regions. This enables us to measure CO intensities with high significance as low as $I_{\rm CO} \approx 0.3$ K km s^{-1} ($\Sigma_{\rm H2} \approx 1$ M$_\odot$ pc^{-2}), an improvement of about one order of magnitude over previous studies. We detect CO out to galactocentric radii $r_{\rm gal} \sim r_{25}$ and find the CO radial profile to follow a remarkably uniform exponential decline with scale length of $\sim$0.2 r_{25}. Here we focus on stacking as a function of radius, comparing our sensitive CO profiles to matched profiles of H I, Hα, FUV, and IR emission at 24 μm and 70 μm. We observe a tight, roughly linear relationship between CO and IR intensity that does not show any notable break between regions that are dominated by molecular gas ($\Sigma_{\rm H2} > \Sigma_{\rm HI}$) and those dominated by atomic gas ($\Sigma_{\rm H2} < \Sigma_{\rm HI}$). We use combinations of FUV+24μm and Hα+24μm to estimate the recent star formation rate (SFR) surface density, $\Sigma_{\rm SFR}$, and find approximately linear relations between $\Sigma_{\rm SFR}$ and $\Sigma_{\rm H2}$. We interpret this as evidence for stars forming in molecular gas with little dependence on the local total gas surface density. While galaxies display small internal variations in the SFR–to–H$_2$ ratio, we do observe systematic galaxy–to–galaxy variations. These galaxy–to–galaxy variations dominate the scatter in relationships between CO and SFR tracers measured at large scales. The variations have the sense that less massive galaxies exhibit larger ratios of SFR–to–CO than massive galaxies. Unlike the SFR–to–CO ratio, the balance between atomic and molecular gas depends strongly on the total gas surface density and galactocentric radius. It must also depend on additional parameters. Our results reinforce and extend to lower surface densities a picture in which star formation in galaxies is separable into two processes: the assembly of star–forming molecular clouds and the formation of stars from H$_2$. The interplay between these processes yields a total gas–SFR relation with a changing slope, which has previously been observed and identified as a star formation threshold.

Subject headings: galaxies: evolution — galaxies: ISM — radio lines: galaxies — stars: formation

1. INTRODUCTION

Stars form out of molecular (H$_2$) gas and many recent observations of nearby galaxies have revealed a strong correlation between the surface density of molecular gas, $\Sigma_{\rm H2}$, and the star formation rate (SFR) surface density, $\Sigma_{\rm SFR}$ (Wong & Blitz 2002; Kennicutt et al. 2007; Bigiel et al. 2008; Leroy et al. 2008; Wilson et al. 2008; Blanc et al. 2009; see also the recent review by Bigiel et al. 2011). These studies show a correlation over several orders of magnitude, but mostly for regions where H$_2$ makes up the majority of the neutral gas, $\Sigma_{\rm H2} \gtrsim \Sigma_{\rm HI}$. The lack of a clear correlation between atomic gas (H I) surface density, $\Sigma_{\rm HI}$, and $\Sigma_{\rm SFR}$ inside galaxy disks (e.g., Bigiel et al. 2008) offers circumstantial evidence that star formation remains coupled to the molecular, rather than total (H I+H$_2$), gas surface density even where H I makes up most of the interstellar medium (ISM). However, the exact relationship between $\Sigma_{\rm SFR}$ and $\Sigma_{\rm H2}$ in the H I–dominated parts of galaxies ($\Sigma_{\rm H2} \lesssim \Sigma_{\rm HI}$) remains largely unexplored.

In this paper we use new, sensitive, wide–field CO maps from the IRAM[12] HERACLES survey (Leroy et al. 2009) to measure correlations between molecular gas and SFR tracers over a large dynamic range. By employing stacking techniques based on H I priors we extend our observations from H$_2$–dominated galaxy centers to the outer parts of galaxies where the H$_2$ surface density is

---

[1] Max-Planck-Institut für Astronomie, Königstuhl 17, 69117 Heidelberg, Germany; schruba@mpia.de
[2] National Radio Astronomy Observatory, 520 Edgemont Road, Charlottesville, VA 22903, USA
[3] Department of Astronomy, Radio Astronomy Laboratory, University of California, Berkeley, CA 94720, USA
[4] Centre for Astrophysics Research, University of Hertfordshire, Hatfield AL10 9AB, U.K.
[5] Astrophysics, Cosmology and Gravity Centre, Department of Astronomy, University of Cape Town, Private Bag X3, Rondebosch 7701, South Africa
[6] IRAM, Avenida Divina Pastora 7, 18012 Granada, Spain
[7] Department of Physics and Astronomy, University of British Columbia Okanagan, 3333 University Way, Kelowna, BC V1V 1V7, Canada
[8] IRAM, 300 rue de la Piscine, 38406 St. Martin d'Hères, France
[9] Observatorio Astronómico Nacional, C/ Alfonso XII, 3, 28014, Madrid, Spain
[10] MPIfR, Auf dem Hügel 69, 53121 Bonn, Germany
[11] Hubble Fellow

[12] IRAM is supported by CNRS/INSU (France), the MPG (Germany) and the IGN (Spain).

much lower than the H I surface density, $\Sigma_{\rm H2} \ll \Sigma_{\rm HI}$.

Deep CO measurements allow us to test if a single "star formation law" applies in both the H_2– and H I–dominated parts of galaxies. Following Schmidt (1959), astronomers have investigated scaling relations linking gas and star formation for decades. Such relations only approximate the complex physical processes involved in star formation but provide useful constraints on theoretical models and important input to simulations. After Kennicutt (1989, 1998), power laws linking surface densities of gas and SFR are the most common formulation. However, the choice of which gas surface density to use — total or molecular gas — remains controversial, as does the extension of any measured molecular relation to low surface densities. The underlying question is what limits star formation in low column density regions, the formation of molecular gas or the efficiency at which the available molecular gas is converted into stars? Sensitive observations of molecular gas down to low surface densities in a large sample of galaxies are needed to address these questions.

Our CO measurements also allow us to investigate the distribution of molecular gas out to large radii. A characteristic exponential decline has been observed several times (Young et al. 1995; Regan et al. 2001; Leroy et al. 2009), but it is not known if this decline becomes sharper at one point, for example corresponding to claimed star formation thresholds (e.g., Martin & Kennicutt 2001). We also test how variations in the H_2–to–H I ratio extend to low surface densities. This quantity is a strong and systematic function of environment in nearby galaxies (Wong & Blitz 2002; Blitz & Rosolowsky 2006; Leroy et al. 2008; Hitschfeld et al. 2009) but it has been difficult to extend the observed correlations to low surface densities.

In Section 2 we describe our sample and data. In Section 3 we present the method that we use to extract sensitive CO measurements. In Section 4 we present radial profiles of H I, CO, IR, FUV, and Hα and use these to relate CO, H I, and tracers of recent star formation. In Section 5 we summarize our results.

2. SAMPLE & DATA

We study 33 nearby, star–forming disk galaxies, the set of HERACLES targets for which we could collect the necessary H I, IR, FUV, and Hα data. This is mainly the overlap of several surveys: HERACLES (IRAM 30m CO, Leroy et al. 2009), THINGS (VLA H I, Walter et al. 2008), SINGS or LVL (*Spitzer* IR, Kennicutt et al. 2003a; Dale et al. 2009), and the GALEX NGS (GALEX FUV, Gil de Paz et al. 2007). We supplement these with a combination of archival and new H I data and archival GALEX data. We exclude low mass, low metallicity galaxies with only upper limits on CO emission and nearly edge–on galaxies.

TABLE 1
Properties of Galaxy Sample

Galaxy	Morph.	D Mpc	Incl. °	P.A. °	r_{25} ′	Metal.[c] 12+logO/H
NGC337	SBd	24.7	51	90	1.48	8.51
NGC628[a,b]	Sc	7.3	7	20	4.92	8.68
NGC925[a,b]	SBcd	9.2	66	287	5.32	8.52
NGC2146	SBab	12.8	54	123	2.69	8.68[d]
NGC2403[a]	SBc	3.2	63	124	7.87	8.57
NGC2798[a]	SBa	24.7	85	152	1.20	8.69
NGC2841[a,b]	Sb	14.1	74	153	3.45	8.87
NGC2903[a,b]	SBd	8.9	65	204	5.92	8.90
NGC2976[a,b]	Sc	3.6	65	335	3.60	8.67
NGC3049	SBab	8.9	58	28	1.04	8.82
NGC3077[a]	Sd	3.8	46	45	2.70	8.64
NGC3184[a,b]	SBc	11.1	16	179	3.70	8.83
NGC3198[a,b]	SBc	13.8	72	215	3.24	8.62
NGC3351[a,b]	SBb	10.1	41	192	3.60	8.90
NGC3521[a,b]	SBbc	10.7	73	340	4.16	8.70
NGC3627[a]	SBb	9.3	62	173	5.14	8.67
NGC3938	Sc	12.2	14	15	1.77	8.74
NGC4214[a,b]	Irr	2.9	44	65	3.40	8.25
NGC4254	Sc	20.0	32	55	2.51	8.79
NGC4321	SBbc	14.3	30	153	3.01	8.83
NGC4536	SBbc	14.5	59	299	3.54	8.61
NGC4559	SBcd	11.6	65	328	5.24	8.55
NGC4569	SBab	20.0	66	23	4.56	8.92
NGC4579	SBb	20.6	39	100	2.51	8.88
NGC4625	SBmp	9.5	47	330	0.69	8.70
NGC4725	SBab	9.3	54	36	4.89	8.73
NGC4736[a,b]	Sab	4.7	41	296	3.87	8.66
NGC5055[a,b]	Sbc	10.1	59	102	5.93	8.77
NGC5194[a]	SBc	8.0	20	172	3.85	8.86
NGC5457[a]	SBcd	7.4	18	39	11.99	8.46[e]
NGC5713	Scd	26.5	48	11	1.23	8.64
NGC6946[a,b]	SBc	5.9	33	243	5.70	8.72
NGC7331[a,b]	Scd	14.7	76	168	4.59	8.68

[a] Targets of THINGS survey (Walter et al. 2008)
[b] Targets in first HERACLES survey paper (Leroy et al. 2009)
[c] Oxygen abundance from Moustakas et al. (2010)
[d] Oxygen abundence from Engelbracht et al. (2008)
[e] Oxygen abundance from Kennicutt et al. (2003b)

Table 1 lists our sample along with adopted morphology, distance, inclination, position angle, optical radius, and metallicity. These values are taken from Walter et al. (2008) if possible and from LEDA and NED in other cases. We quote oxygen abundances (metallicities) from Moustakas et al. (2010, Table 9), averaging the metallicities derived from a theoretical calibration (their KK04 values) and an empirical calibration (their PT05 values). For galaxies without a Moustakas et al. (2010) metallicity, we adopt a metallicity equal to the average of their B–band luminosity–metallicity relations. For NGC 2146 we quote the metallicity given by Engelbracht et al. (2008). For NGC 5457 (M 101) we take a constant metallicity defined by the value at 0.4 r_{25} from the gradient fit by Kennicutt et al. (2003b).

We trace molecular hydrogen (H_2) using CO($2 \rightarrow 1$) line emission observed with the IRAM 30m as part of the HERACLES survey (Leroy et al. 2009). They describe in detail the observations and reduction for the subset of galaxies observed until Summer 2008. The remaining targets were observed and reduced in the same way. The final data cubes have an angular resolution (FWHM) of 13″ and a spectral resolution (channel separation) of 2.6 km s^{-1}.

Our measurements of atomic hydrogen (H I) come mostly from the THINGS survey (Walter et al. 2008), which used the Very Large Array [13] (VLA) to observe the 21-cm hydrogen line in 34 nearby galaxies. The observing and reduction strategies are described therein. The

---

[13] The National Radio Astronomy Observatory is a facility of the National Science Foundation operated under cooperative agreement by Associated Universities, Inc.

final data cubes have an angular resolution of $\sim 11''$ (using natural weighting) and a spectral resolution of 2.6 or 5.2 km s^{-1}. THINGS is sensitive to $\Sigma_{\rm HI} \approx 0.5$ M$_\odot$ pc^{-2} on scales of $30''$. Using azimuthal averaging, we reach even better sensitivities at large radii. As a result, the H I sensitivity never limits our analysis.

The H I data for NGC 337, 2146, 2798, 3049, 3938, 4254, 4321, 4536, 4579, 4625, 4725, and 5713 are a combination of new and archival VLA data (the new data are from VLA programs AL731 and AL735). These have been reduced and imaged using the Common Astronomy Software Applications (CASA) following a similar protocol than the THINGS reduction. These supplemental H I cubes include only data from the VLA's C and D configurations; THINGS also includes B configuration data. For NGC 4559 we take H I data observed with the Westerbork Synthesis Radio Telescope (WSRT) by van der Hulst (2002). The beam sizes (FWHM) of the supplemental H I are $15''-25''$ and the velocity resolution is $2.5-20$ km s^{-1}, usually 10 km s^{-1}.

We derive H I surface densities from 21-cm line intensities and H$_2$ surface densities from CO($2 \rightarrow 1$) line intensities following

$$\Sigma_{\rm HI} = 0.02\ I_{\rm HI} \times \cos\ i \qquad (1)$$

$$\Sigma_{\rm H2} = 6.25\ I_{\rm CO} \times \cos\ i \qquad (2)$$

where $\Sigma_{\rm HI}$ and $\Sigma_{\rm H2}$ have units of M$_\odot$ pc^{-2} and $I_{\rm HI}$ and $I_{\rm CO}$ are measured in K km s^{-1}. The mass surface densities are projected to face–on values and include a factor of 1.36 to account for heavy elements. For Equation (2) we have assumed a CO line ratio of $I_{\rm CO}(2 \rightarrow 1)/I_{\rm CO}(1 \rightarrow 0) = 0.7$ and a CO($1 \rightarrow 0$)–to–H$_2$ conversion factor $X_{\rm CO} = 2.0 \times 10^{20}$ cm^{-2} (K km s^{-1})$^{-1}$ (see Leroy et al. 2009, and references therein).

We use broadband infrared (IR) photometry at 24 μm and 70 μm obtained by the *Spitzer* legacy surveys SINGS (Kennicutt et al. 2003b) and LVL (Dale et al. 2009). *Spitzer* has angular resolution $\sim 6''$ at 24 μm and $18''$ at 70 μm. The sensitivity of these data is sufficient to obtain high signal–to–noise measurements when averaging in radial rings (see below) throughout the area that we study ($r_{\rm gal} \lesssim 1.2\ r_{25}$).

The GALEX NGS (Gil de Paz et al. 2007) imaged far– and near–ultraviolet (FUV and NUV) emission for most of our targets. The FUV band covers $1350-1750$ Å with an angular resolution $\sim 4.5''$. We use these images to trace unobscured emission from young stars. For galaxies not covered by the NGS, we searched the NASA Multimission Archive at STScI and used the FUV image with the longest exposure time. These data also have sufficient sensitivity to determine FUV intensities with high signal–to–noise throughout the star–forming disk.

We draw Hα data from the SINGS and LVL surveys, complemented by literature data for NGC 2903, 4214, 4569, 4736, and 5457. For the literature and several problematic SINGS targets, we pin the total Hα+[N II] flux to published values, usually those of Kennicutt et al. (2008). Leroy et al. (2011, in prep.) describe the processing of the maps, which involves subtracting a smooth background, masking foreground stars following Muñoz-Mateos et al. (2009), correcting for [N II] contamination following Kennicutt et al. (2008), and correcting for Galactic extinction. The Hα maps become uncertain, and likely biased low due to background subtraction, below intensities equivalent to $\Sigma_{\rm SFR}$ of a few times 10^{-4} M$_\odot$ yr^{-1} kpc^{-2}, values typically crossed inside the radial range studied here. This, and the declining Hα–to–FUV flux ratios which are observed as *Galex* UV disks extending far beyond the Hα emission (Thilker et al. 2007; Meurer et al. 2009), limit the utility of the Hα maps to trace star formation in the low brightness regions of outer galaxy disks.

After we examine correlations among observables, we will estimate the star formation rate surface density, $\Sigma_{\rm SFR}$, from combinations of Hα with 24 μm (Kennicutt et al. 2007) and FUV with 24 μm (Leroy et al. 2008). We adopt the Hα+24μm calibration by Calzetti et al. (2007) and the FUV+24μm combination from Leroy et al. (2008),

$$\Sigma_{\rm SFR(H\alpha+24)} = \left(2.9\times10^{-2}\ I_{\rm H\alpha} + 2.5\times10^{-3}\ I_{24\mu{\rm m}}\right) \times \cos\ i \qquad (3)$$

$$\Sigma_{\rm SFR(FUV+24)} = \left(8.1\times10^{-2}\ I_{\rm FUV} + 3.2\times10^{-3}\ I_{24\mu{\rm m}}\right) \times \cos\ i \qquad (4)$$

where $\Sigma_{\rm SFR}$ has units of M$_\odot$ yr^{-1} kpc^{-2} and Hα, FUV, and 24 μm intensities are all in MJy sr^{-1}. Both $\Sigma_{\rm SFR}$ calibrations combine a tracer of the unobscured star formation with infrared (24 μm) emission, which is intended to trace young starlight reprocessed by dust. Hα traces O stars with ages $\lesssim 5$ Myrs (Kennicutt et al. 2009) with sensitivity out to ~ 10 Myr (Vacca et al. 1996). FUV traces O and B stars of typical age $20-30$ Myrs with sensitivity out to ~ 100 Myr (Salim et al. 2007).

Our use of both Hα+24μm and FUV+24μm emission gives some test of sensitivity to our choice of star formation rate tracer. Several other concerns are worth mentioning. Because dust properties and the stellar populations heating the dust somewhat differ between H II regions and large (kpc) regions in galaxies the appropriate weighting of the 24 μm emission to correct for extinction may be a function of scale and environment. The dust–to–gas ratio, dust size–distribution, ISM geometry, and recent star formation history may also play important roles. The Calzetti et al. (2007) calculation remains state of the art, but there is no definitive consensus about the correct calibration to use outside bright regions that they study. The reliability of the Hα imaging at low surface brightness also represents a concern. Ground based, narrowband Hα imaging is challenging and the Hα+24μm tracer must be considered unreliable where $\Sigma_{\rm SFR(H\alpha)} \approx 5 \times 10^{-4}$ M$_\odot$ yr^{-1} kpc^{-2}. The *Galex* and *Spitzer* maps are better behaved at low surface brightness.

Because of these data quality considerations and our focus on regions with low surface brightness, we emphasize comparisons to FUV+24μm. SFR(FUV+24) and SFR(Hα+24) give comparable results with scatter of only 0.1 dex ($\sim$25%) down to $\Sigma_{\rm SFR} \sim 5 \times 10^{-4}$ M$_\odot$ yr^{-1} kpc^{-2} in an azimuthally averaged ring. Our main method to address these other systematic concerns is to emphasize the observed scaling relations in the first

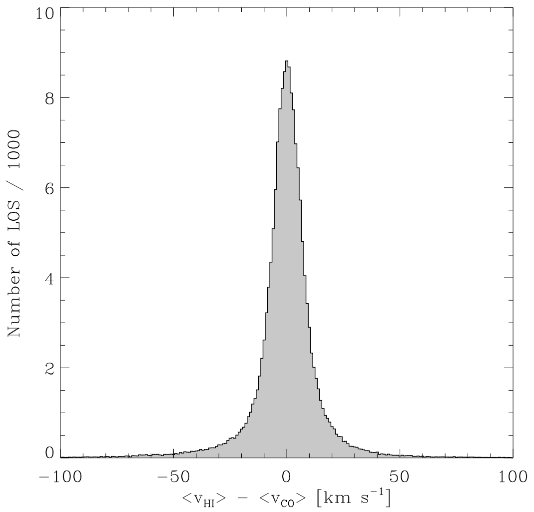

FIG. 1.— The difference between local mean velocities of H I and CO for lines of sight with galactocentric radius smaller than 0.5 r_{25}. The close correspondence motivates our use of the H I mean velocity to predict the CO velocities in low surface brightness regions.

part of the paper. For a more thorough discussion of hybrid SFR tracers see Kennicutt et al. (2009) and for a discussion of their application to gas–SFR comparisons, we refer the reader to Leroy et al. (2011, in prep.).

3. METHODOLOGY

Our goal is to recover low brightness CO emission from the outer parts of galaxies. CO is very faint in these regions and individual spectra have low signal–to–noise ratios (SNR), requiring us to average many spectra to achieve a detection. Because the velocity of CO emission varies with position, simply averaging spectra spreads the emission across many velocity channels with low SNR in each channel. In principle, this could still yield a high SNR measurement. In practice we wish to maximize SNR by considering only the part of each spectrum likely to contain emission. We must also contend with systematic effects of weather, receiver instabilities, and dish imperfections. These all induce frequency–dependent behavior (“baselines problems”) that make a clear detection of an emission line an important step in a robust analysis.

With these issues in mind, we use the following technique to average CO spectra across large parts of a galaxy. First, we estimate the local mean velocity of CO emission from the H I data. Using this mean velocity, we redefine the velocity axis of each CO spectrum so that the local mean velocity is now zero. We average these shifted CO spectra from across our target region. In the averaged spectra we expect the CO line to emerge at zero velocity with good SNR. The baseline problems described above will not average coherently, allowing a straightforward identification of the line.

This approach hinges on the assumption that the H I mean velocity is a good proxy for the mean velocity of the molecular gas. Figure 1 shows that this assumption holds where we detect CO over individual lines of sight, with median $\bar{v}_{\rm CO} - \bar{v}_{\rm HI}$ of -0.22 km s^{-1} and a 1σ dispersion of 7.0 km s^{-1}. We expect a similar correspondence in the outer, CO–faint parts of galaxies.

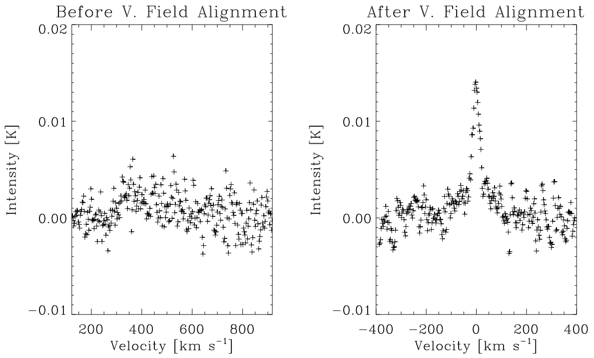

FIG. 2.— Average CO spectrum across tilted ring spanning from $0.7 - 0.8$ r_{25} in NGC 5055. The left panel shows the result of a simple average of all spectra. The right panel shows the average after each spectrum is shifted so that $v = 0$ corresponds to the local mean H I velocity.

Leveraging H I to detect CO at large radii works because the H I surface densities are essentially constant out to large radii, making H I easily detected across galaxy disks. CO emission, on the other hand, tends to be bright in galaxy centers but declines rapidly with increasing galactocentric radius.

3.1. *Stacking of CO Spectra*

Predicting the velocity of the CO line from the H I data allows us to increase the SNR when measuring the integrated CO intensity. The HERACLES bandpass is ∼1000 km s^{-1} and a typical CO line width at large galactocentric radii is ∼25 km s^{-1}. The H I allows us to restrict our integration to just the relevant part of the spectrum which represents a substantial gain in sensitivity.

Just as important as the increase in SNR, the shifted and stacked spectra allow us to verify that faint emission is actually an astronomical signal. Even for faint CO emission the stacking technique has the potential to reveal a spectral line. Low–level variations due to weather, receiver instabilities, and other systematic effects in the telescope will not create such an effect. Even stray pickup of astronomical emission due to surface imperfections (i.e., error beam effects) will emerge at a low level offset from zero velocity due to galaxy rotation.

Figure 2 demonstrates this approach. We plot the averaged CO spectrum of NGC 5055 inside a tilted ring spanning from $0.7 - 0.8$ r_{25}. In the left panel the spectra were averaged as they were observed, whereas in the right panel we first shifted by the local H I mean velocity and then averaged. Both spectra contain the same integrated intensity, however, only the appearance of a clear line feature in the right spectrum at the expected velocity strongly indicates that the signal is not due to baseline features but cannot be anything but CO emission.

3.2. *Fitting the CO Line*

To extract CO line emission, we perform an automated line fit to each stacked spectrum. This approach picks out spectral line emission rather than baseline structure and does not require us to define an integration window beforehand.

In most regions, the line can be well–approximated by a Gaussian profile with FWHM of ∼$15 - 40$ km s^{-1} (Figure 3 upper right panel). However, in the central regions of some galaxies the line can be very broad with a flat-

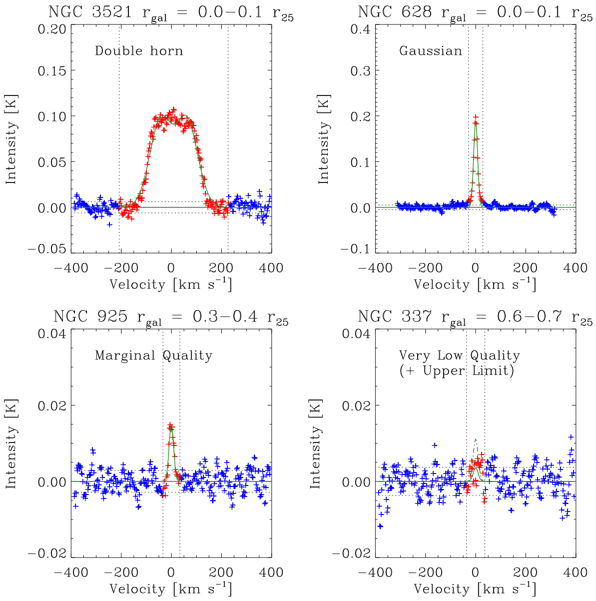

Fig. 3.— Examples of stacked CO spectra with different line shapes. The upper row shows spectra with high quality fits and the lower row shows spectra with low quality fits. The horizontal dotted lines mark the 1σ rms noise of the stacked spectrum. The *upper left* panel shows a broad line approximated by a double–horn profile. The *upper right* panel shows a narrow line fitted by a Gaussian. The *lower left* panel shows a marginal quality fit. The *lower right* panel shows a low quality fit together with the associated upper limit (dashed line).

tened or double–horned peak (Figure 3 upper left panel). These profiles often coincide with central enhancements like bars or molecular rings and are poorly parametrized by a single Gaussian. Instead we fit a double–horn profile, a Gaussian scaled by a symmetric second–order polynomial (functional form from Saintonge 2007). Based on “by eye” inspection, the asymmetry in these profiles is small enough that a symmetric function is sufficient.

We derive the best fit profile via a non–linear least squares fit[14]. We constrain the fit parameters so that the center of the profile lies within ±50 km s^{-1} of zero velocity after shifting, the FWHM is larger than 15 km s^{-1} (to avoid the fit latching onto individual channels), and the amplitude is positive. We always carry out a Gaussian fit first and in those cases where the FWHM exceeds 60 km s^{-1} we switch to a double–horn profile. We verify by eye that this yields sensible results.

The integral of the fitted profile gives us the integrated CO line intensity. We derive the uncertainty in this quantity from the noise, estimated from the signal–free part of the spectrum, and the width of the profile. It proved useful to define a quality scale for the fit. The quality is “high” where the peak intensity is larger than 5σ and its integrated intensity is larger than 10 times its uncertainty. In cases where the peak intensity is less than 3σ or the integrated intensity is less than 5 times its uncertainty, we do not trust the fit and instead determine an upper limit. We label cases that fall between these regimes as “marginal”. Figure 3 shows examples of our quality measures and line profile fits.

We derive our upper limits integrating over a Gaussian line profile with FWHM set to 18 km s^{-1}, the typical FWHM found for high SNR spectra at $r > 0.5\ r_{25}$, and fixed amplitude of 3σ.

3.3. *Stacking as a Function of Radius*

We present our stacking technique applied to radial bins. In principle this method allows us to stack spectra across any region. For example, we could define regions by total gas column, infrared intensity, or features such as spiral arms and bars. In practice, radius makes an excellent ordinate. We wish to study the underlying relationship between CO, H I, IR, FUV, and Hα intensity. Stacking with one of these quantities as the ordinate would require carefully modeling the biases involved to measure the underlying relationships. Galactocentric radius is a well–determined, independent quantity that is also highly covariant with these other intensities. This yields a dataset with large dynamic range that is easy to interpret.

Therefore we focus our analysis on data stacked in bins of galactocentric radius. We average over tilted rings 15″ wide, comparable to the angular resolution of our data. This width corresponds to ∼220 pc for our nearest targets (3 Mpc) and ∼1800 pc for our most distant targets (25 Mpc). We construct the rings assuming that each galaxy is a thin disk with the inclination and position angle given in Table 1. To measure CO with highest sensitivity we construct stacked CO spectra using the procedure described above and fit those to determine the integrated CO line intensities. For the other observables — H I, IR, FUV, and Hα intensities — we use two–dimensional maps of intensity and determine the mean intensity for each tilted ring.

Error bars on the H I, IR, FUV, and Hα intensities show the 1σ scatter within that tilted ring, capturing both statistical noise and deviations from axial symmetry. We estimate the 1σ scatter for our CO measurements by integrating the CO cube over a velocity window that is adjusted for each line of sight such that it includes all channels of significant CO emission but at least all channels with velocities within 25 km s^{-1} of the local mean H I velocity. Note that our 1σ values reflect the scatter in (integrated) intensities of individual lines of sight inside a ring. They should not be confused with the uncertainty in the determination of the mean intensity inside a ring which is typically much smaller.

4. RESULTS

In Figure 4 for NGC 628 and in the Appendix for the rest of the sample, we present stacked radial profiles of integrated CO intensity along with profiles of H I, infrared intensity at 24 μm and 70 μm, FUV, and Hα intensity. Following Equations (3) we combine Hα and 24 μm intensities to estimate the star formation rate surface density SFR(Hα+24) and compare those to SFR(FUV+24) derived from FUV and 24 μm intensities using Equation (4).

For each galaxy there are two plots: The left panel shows H I, H$_2$ (from CO), and SFR for both FUV+24μm and Hα+24μm. The right panel shows our SFR tracers — Hα, FUV, 24 μm and 70 μm emission. We present

---

[14] We use the IDL procedure `MPFIT.PRO` from Craig Markwardt which performs a Levenberg–Markwardt non–linear least squares minimization and is based on the `MINPACK-1 LMDIF.F` algorithm from More et al. (1978)

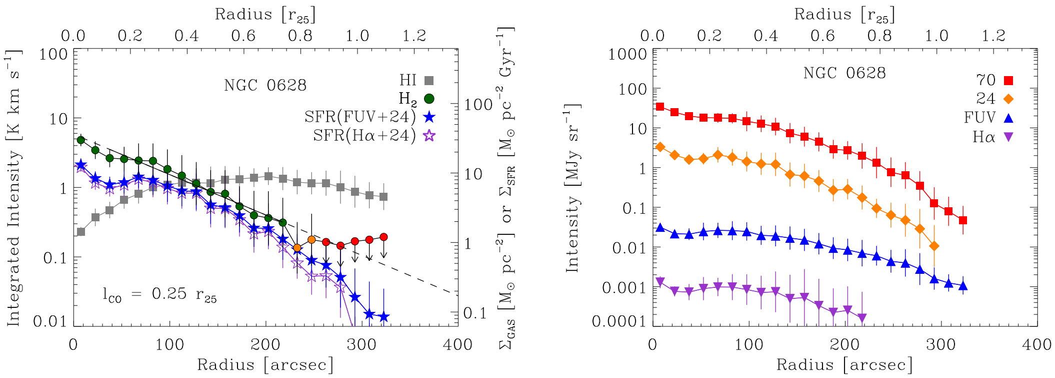

FIG. 4.— Azimuthally averaged intensity in 15″ wide tilted rings in NGC 628: (*left*) H I, H$_2$, and SFR from FUV+24μm and Hα+24μm; (*right*) 24 μm, 70 μm, FUV, and Hα intensity. Left–hand y–axes show observed intensities, the right–hand y–axis shows the surface densities of H I, H$_2$, and SFR projected to face–on values. The color of the CO points indicates the significance of the fit to the stacked spectrum: high quality in green, marginal quality in orange, and upper limits in red. The solid–dashed line shows an exponential fit to the radial CO profile with the scale length, $l_{\rm CO}$, printed in the lower left corner. Error bars show the 1σ scatter inside each tilted ring. Note that we have scaled the H I intensities (left y–axis) by a factor of 312.5 in order to match all profiles in units of surface density (see text).

the profiles in both observed intensity[15] (left hand y–axis) and units of surface density (right hand y–axis of the left panel) — $\Sigma_{\rm H2}$, $\Sigma_{\rm HI}$, and $\Sigma_{\rm SFR}$. Note that we have projected (only) the surface densities of H I, H$_2$, and SFR to face–on values (i.e., we corrected for inclination). The observed surface brightnesses are not corrected for the effect of inclination. Such a correction will just move each galaxy up and down in lockstep and we find it more useful to report the observed values. The color of a point in the CO profile indicates the significance of the fit to the stacked spectrum: green for high significance, orange for marginal significance, and red for upper limits, these correspond to 3σ upper limits on the fitted intensity (see Section 3.2).

4.1. *CO and Star Formation*

With these azimuthally averaged data we are able to compare CO to tracers of recent star formation across a large range of H$_2$–to–H I ratios. In this subsection, we make empirical comparisons between measured intensities, examine the relative roles of H$_2$ and H I in the "star formation law," and investigate the origin of the scatter in these relations.

4.1.1. *Scaling Relations between CO and IR, FUV, and Hα*

Figures 5 & 6 show scaling relations between observed intensities of CO (x–axis) and different tracers of recent star formation (y–axis). Figure 5 shows infrared intensities at 24 μm (top panels) and 70 μm (bottom panels) and Figure 6 shows intensities of FUV (top panels) and Hα (bottom panels). The left hand panels show the relations for all galaxies and all radii. The panels on the right hand side show only radii $r > 0.5\ r_{25}$. H$_2$ and H I make up roughly equal parts of the ISM near this radius (see the left panel of Figure 13), so most of the points in the right hand panels are H I–dominated. A dotted vertical line shows an integrated CO intensity of 2.2 K km s^{-1}, which corresponds to $\Sigma_{\rm H2} \approx 10$ M$_\odot$ pc^{-2} (assuming $i = 45°$), which is about the surface density at which H$_2$ and H I make up equal parts of the ISM. A dashed vertical line at $I_{\rm CO} = 0.3$ K km s^{-1} ($\Sigma_{\rm H2} \approx 1$ M$_\odot$ pc^{-2} for $i = 45°$) shows a conservative sensitivity limit for the whole sample. Typically our upper limits, which are not displayed in these plots, lie to the left of this line. They will be systematically higher at large radii when radial rings partially exceed the coverage of our CO maps.

CO emission correlates tightly with IR emission at 24 μm and 70 μm (Figure 5) (rank correlation coefficient $r_{\rm corr} = 0.9$). The correlation extends over three orders of magnitude in CO and IR intensities and crosses the H I–to–H$_2$ transition without substantial change in slope or normalization. Comparing the left panels (all radii) and the right panels ($r > 0.5\ r_{25}$) does not reveal any significant radial dependence.

CO emission exhibits a weaker correlation with FUV and Hα (Figure 6) ($r_{\rm corr} = 0.5 - 0.6$) than with IR emission, i.e., both the CO–FUV and CO–Hα relation show much larger scatter than the CO–IR relations. The CO–FUV relation displays a break between H I– and H$_2$–dominated regimes. The increased scatter and weaker correlation at least partially reflects the sensitivity of Hα and FUV emission to absorption by dust. In the inner ($r \lesssim 0.5\ r_{25}$), more gas rich parts of galaxies dust reprocesses most Hα and FUV emission into IR emission. In this regime CO and FUV are to first order uncorrelated ($r_{\rm corr} = 0.16$). Outside $\sim$0.5 r_{25} the filling factors of dense gas and dust are lower and FUV is less affected by extinction. The correlation coefficient between CO and FUV or Hα is $r_{\rm corr} = 0.45 - 0.55$ in this regime, still not as high as for the whole galaxies because of the limited dynamic range in intensity. In Section 4.1.2 we will see that the weaker correlation of CO with Hα and FUV is mostly due to galaxy–to–galaxy variations, possibly reflecting different star formation histories, dust abundances, geometries, and potential changes in the CO–to–H$_2$ conversion factor.

We use the ordinary least squares (OLS) bisector to fit power laws to each relation. In terms of sensitivity to a given amount of star formation, the SFR tracers are much more sensitive than our CO maps. To properly fit a relation between them we thus need to either carefully incorporate upper limits (e.g., see Blanc et al. 2009) or

---

[15] In order to have H I and H$_2$ comparable in units of mass surface density we scale the observed H I intensity by a factor of 312.5; the ratio of Equation (1) and (2).

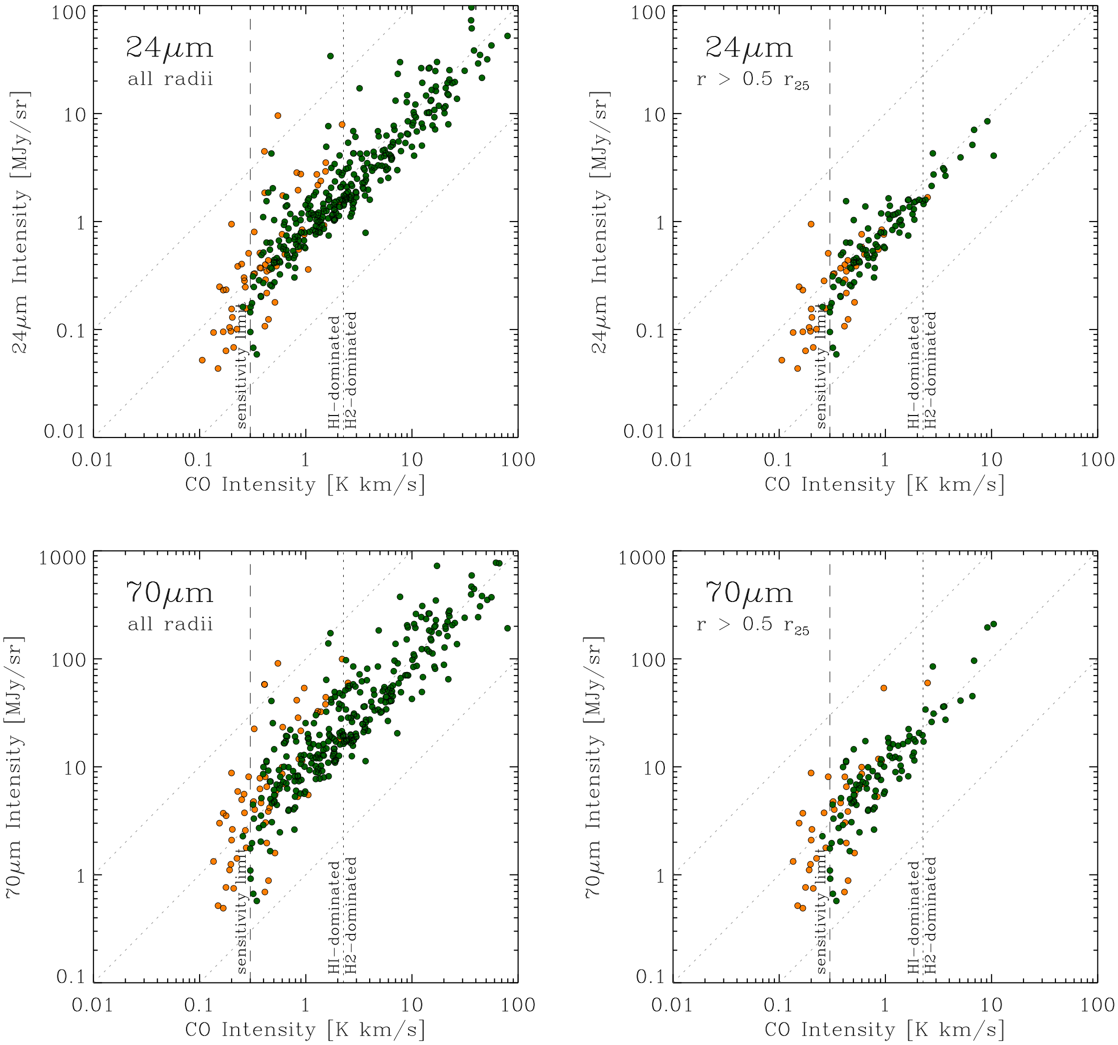

Fig. 5.— Observed IR intensities (y–axis) as a function of integrated CO($2 \rightarrow 1$) intensity (x–axis). Each point corresponds to a stacked average in a tilted ring $15''$ wide. Green and orange symbols indicate CO measurements of high or marginally significance; radial rings with only upper limits on the CO intensity (not shown here) are located exclusively to the left of the long–dashed line. The top panels shows the relation of 24 μm versus CO, the bottom panels shows 70 μm versus CO. The left panels show data for all radii, whereas the right panels show only data outside 0.5 r_{25}, where the ISM is typically H I–dominated. The short–dashed vertical line indicates a typical CO intensity at which $\Sigma_{\rm H2} \sim \Sigma_{\rm HI}$; data to the left of this line will usually be H I–dominated. The diagonal dashed lines indicate lines of constant ratios for orientation.

impose a matched sensitivity cut on the SFR tracer data. We take the latter approach, discarding data below 0.1, 1.0, 10^{-3}, and 10^{-4} MJy sr^{-1} at 24 μm, 70 μm, FUV, and Hα intensities after an initial fit[16]. Graphically, this removes the flaring towards low intensity just above our sensitivity cut seen in Figure 5 & 6, because we are not sensitive to a similar flaring towards low CO intensities.

Table 2 reports these fits considering all regions with CO measurements of high significance and SFR tracers above the sensitivity cut. The main result is that CO emission is consistent with being linearly proportional to IR emission both at 24 μm and 70 μm, down to low surface brightness. The best fits relating CO with FUV or Hα emission are also consistent with a linear slope within the large uncertainties, but power laws are clearly an inadequate description of those data.

4.1.2. *Scatter in the Scaling Relations*

Each of the observed relations displays significant scatter: $I_{24\mu\rm m}/I_{\rm CO}$ has 1σ scatter of about 0.17 dex ($\sim$50%) and $I_{70\mu\rm m}/I_{\rm CO}$ scatters by 0.24 dex ($\sim$75%), whereas $I_{\rm H\alpha}/I_{\rm CO}$ scatters by 0.34 dex (a factor of 2.2) and $I_{\rm FUV}/I_{\rm CO}$ by 0.55 dex (a factor of 3.5). The origin of this scatter is of astrophysical interest. On small scales, this scatter arises from the evolution of individual star–forming regions, which vary dramatically in their ratios of CO–to–SFR tracers — leading to a breakdown of scaling relations when a resolution element corresponds to an individual region (Schruba et al. 2010). Here our azimuthal averaging washes out such small–scale variations. Each point averages over many individual star–forming regions. However, we do have the ability to

---

[16] The result is relatively insensitive to the exact choice of sensitivity cut. Varying it by a factor of 2 affects the power law index by $\sim$0.05 for the CO–IR relations and $\sim$0.15 for CO–FUV or CO–Hα.

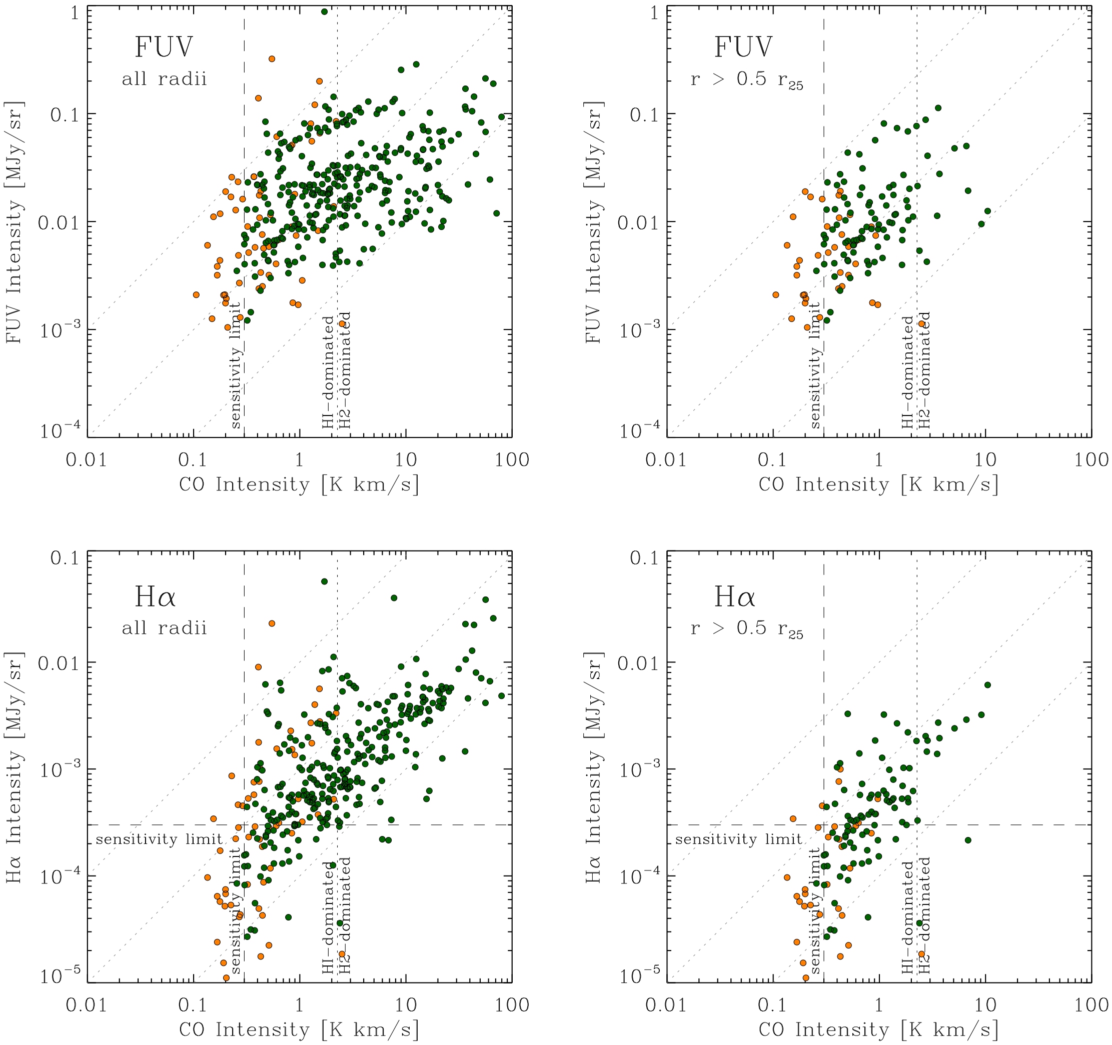

FIG. 6.— A similar plot as Figure 5 but this time showing the relation of FUV versus CO and Hα versus CO for our two radial ranges. Note that Hα intensities below a few times 10^{-4} MJy sr^{-1} are affected by data quality and processing and have to be considered uncertain.

TABLE 2
RELATION OF IR EMISSION AND SFR TRACERS TO CO

SFR Tracer	Rank Correlation	Power Law Index
24 μm		
... all data	0.90 ± 0.05[a]	1.0 ± 0.1[b]
... $r > 0.5\ r_{25}$	0.87 ± 0.10	1.1 ± 0.1
70 μm		
... all data	0.87 ± 0.05	1.0 ± 0.1
... $r > 0.5\ r_{25}$	0.84 ± 0.10	1.1 ± 0.2
FUV		
... all data	0.47 ± 0.05	0.8 ± 0.6
... $r > 0.5\ r_{25}$	0.46 ± 0.09	1.1 ± 0.8
Hα		
... all data	0.63 ± 0.05	0.9 ± 0.4
... $r > 0.5\ r_{25}$	0.55 ± 0.10	1.1 ± 0.6

[a] We estimate the uncertainty in the rank correlation coefficient by taking the correlation coefficient derived from 1,000 random pairwise re–orderings of the data.

[b] The slope quoted here is from the ordinary least squares bisector with the error estimated from the spread in fitting x vs. y and y vs. x.

distinguish scatter *within* a galaxy from scatter *among* galaxies.

To investigate the origin of the observed scatter, we remove galaxy–to–galaxy variations from the observed relation. We do so in two ways: First, we fit power–laws relating CO to IR, FUV, or Hα in each galaxy and then adjust all galaxies to have the same normalization. *A priori* we do not know if the galaxy–to–galaxy variations mainly affect the measurement of our gas tracer (x–axis) or the measurements of our SFR tracers (y–axis), therefore, we repeat the exercise matching normalizations at a fixed value in y and then in x. We then compare the scatter among normalizations to the scatter about the re–normalized relation.

We also carry out a more basic test, measuring how the scatter in the ratio of SFR tracer to CO emission varies both among and within galaxies. We compare the scatter in the median ratio of SFR tracer to CO, $\langle I_{24\mu\mathrm{m}}/I_{\mathrm{CO}}\rangle$, among galaxies to the scatter in deviations from this median ratio within galaxies, $I_{24\mu\mathrm{m}}/I_{\mathrm{CO}} - \langle I_{24\mu\mathrm{m}}/I_{\mathrm{CO}}\rangle$.

For both approaches, we find that galaxy–to–galaxy

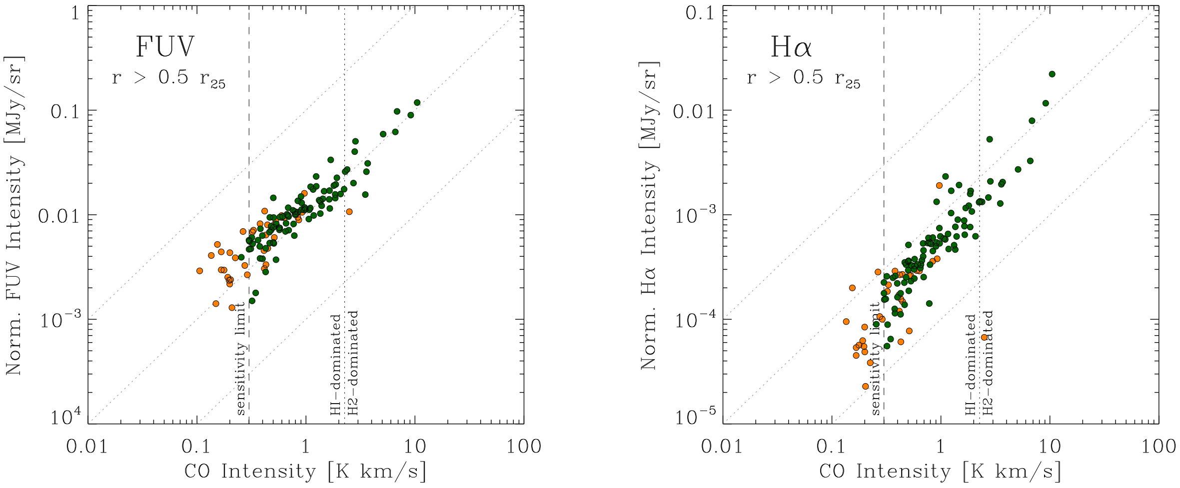

Fig. 7.— Relation between CO intensity and normalized FUV intensity (left panel) and normalized Hα intensity (right panel) for outer disks, $r > 0.5\ r_{25}$. For each galaxy we use power law fits to the data of high quality and normalize the relation by the FUV or Hα intensity, respectively, which the fit has at 1 K km s^{-1}.

variations dominate the scatter in the observed relation. Scatter among galaxies in Figure 5 & 6 is ∼2 times larger than the scatter within individual galaxies. The most striking cases are Hα and FUV emission in the outer parts of galaxies. Figure 7 shows that after normalization, the relation of CO with FUV and Hα emission for radii $r > 0.5\ r_{25}$ becomes very strong ($r_{\rm corr} = 0.9$) and nearly linear (power law index of 0.90 ± 0.05 for FUV and 1.1 ± 0.05 for Hα). Thus in the outer parts of galaxies the FUV–to–CO and the Hα–to–CO ratios vary dramatically among galaxies but are largely fixed inside each galaxy. The scatter appears driven at least in part by real systematic variations in the ratio of CO–to–SFR tracers as a function of other galaxy parameters (see below and Young et al. 1996). The case in the inner parts of galaxies is more complex because of high dust attenuations resulting in non–linear CO–FUV and CO–Hα relations.

4.1.3. *H_2 and Star Formation*

In Figure 8 we combine FUV and 24 μm intensities to estimate $\Sigma_{\rm SFR}$, which we plot as a function of $\Sigma_{\rm H2}$. In Figure 9 we instead combine Hα and 24 μm to estimate $\Sigma_{\rm SFR}$. In both Figures, the left hand panels show data for all radii, while the right hand panels show only rings with $r > 0.5\ r_{25}$, where the ISM is mostly H I. As in Figure 5 & 6, a vertical dotted line shows $\Sigma_{\rm H2} \approx 10$ M$_\odot$ pc^{-2}, a typical H_2 surface density where the ISM consists of equal parts H I and H_2.

In agreement with Bigiel et al. (2008, 2011), we observe an approximately linear scaling of $\Sigma_{\rm SFR}$ and $\Sigma_{\rm H2}$ in regions that are dominated by molecular gas ($\Sigma_{\rm H2} \gtrsim 10$ M$_\odot$ pc^{-2}). For Figure 8 this agreement does not come as a surprise because we use many of the same data and a similar approach (FUV+24μm) to estimate recent SFR. The new results here are that (a) this trend *continues without significant changes* down to very low $\Sigma_{\rm H2}$, including regions strongly dominated by atomic gas, and (b) we find the same trend in Figure 9 using SFR(Hα+24μm).

The rank correlation coefficient relating $\Sigma_{\rm H2}$ and $\Sigma_{\rm SFR}$ for all data with at least a marginal CO measurement is $r_{\rm corr} \approx 0.85$. The scatter about a linear relation is 0.25 dex (prior to any normalization). Both numbers resemble those derived for the CO–24 μm relation in Section 4.1.1 because 24 μm emission drives our hybrid SFR tracer over most of the area. In detail, the fractional contribution of 24 μm to SFR varies with radius and choice of hybrid tracer. Generally speaking: (a) the larger the radius the larger the contribution of the unobscured term, and (b) Hα contributes fractionally more than FUV to the hybrid.

An OLS bisector fit yields a roughly linear slope and a molecular depletion time, $\tau_{\rm dep} = \Sigma_{\rm H2}/\Sigma_{\rm SFR}$, of ∼1.8 Gyr (including a factor 1.36 to account for heavy elements; see Table 3 for fit parameters). This is slightly lower than $\tau_{\rm dep} = 2$ Gyr found by Bigiel et al. (2008) and Leroy et al. (2008) for a subset of the data analyzed here and $\tau_{\rm dep} = 2.35$ Gyr recently found by Bigiel et al. (2011) for a sample that is similar to the one analyzed here. We include (a) more starburst galaxies and (b) more low mass, low metallicity spiral galaxies that Bigiel et al. (2008) and Leroy et al. (2008) excluded from their CO analysis. Both dwarfs and starbursts have shorter $\tau_{\rm dep}$ than large spirals (see below and Kennicutt 1998; Gao & Solomon 2004; Leroy et al. 2008; Daddi et al. 2010). Moreover, our radial profiles weight these small galaxies more heavily than the pixel sampling used by Bigiel et al. (2008, 2011).

As with the scaling relations between CO and tracers of recent star formation (Figure 5 & 6), the H_2–SFR relation exhibits significant scatter. We perform the same procedure to isolate galaxy–to–galaxy variations from scatter within galaxies and again find the scatter in the main relation (upper panels in Figure 8 & 9) dominated by galaxy–to–galaxy variations. We plot the relations after normalization in x and y in the middle and bottom panels of Figure 8 & 9. Once galaxy–to–galaxy scatter is removed, there is a remarkably tight, uniform linear relation linking molecular gas and star formation across almost three and a half orders of magnitude.

What drives this galaxy–to–galaxy variation? In both the H_2–SFR and observed intensity relations a large part of the scatter comes from a sub–population of less massive, less metal–rich galaxies that exhibit high SFR–to–CO ratios. Figure 10 shows the metallicity depen-

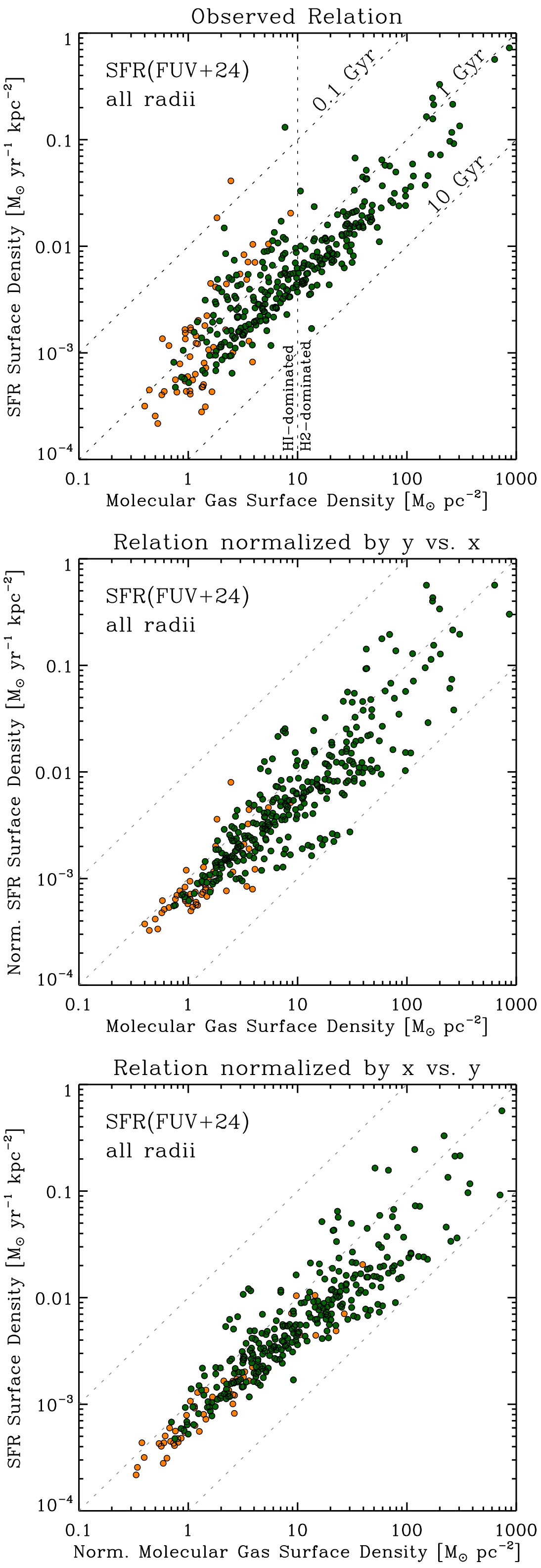

FIG. 8.— Recent star formation rate surface density estimate from FUV+24μm (y–axis) as a function of molecular gas surface density (x–axis). The left–hand column shows data for all radii, whereas the right–hand column shows only data where $r > 0.5\ r_{25}$. The upper row presents the basic relation, which is approximately linear with average H_2 depletion time $\sim$2.0 Gyr (dashed lines). The middle and bottom rows show results after we fit and remove galaxy–to–galaxy variations. These galaxy-to-galaxy variations are $\sim$2 times larger than internal variations, suggesting individual galaxies each obey well–defined, though offset, relations.

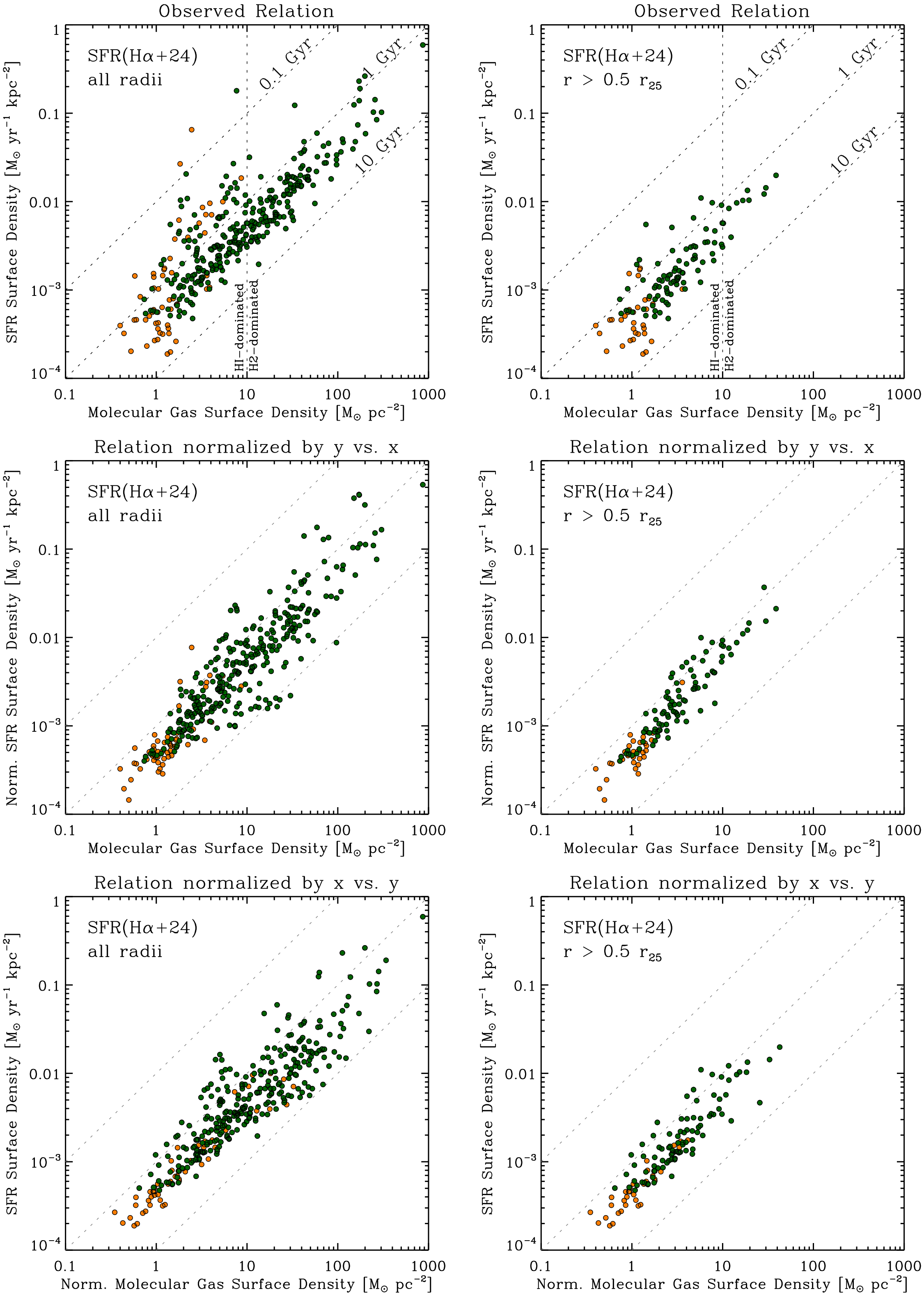

FIG. 9.— The same plot as Figure 8 but this time using Hα+24μm to estimate $\Sigma_{\rm SFR}$.

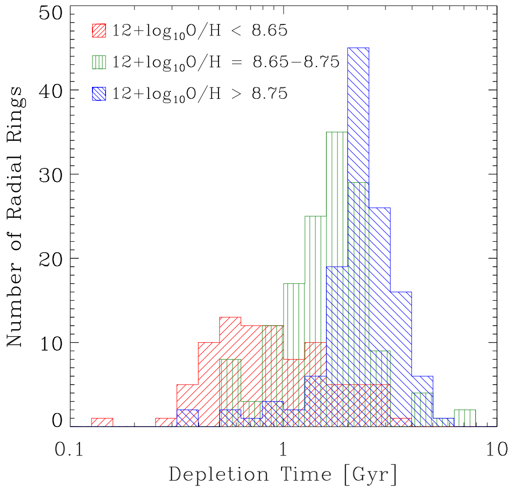

Fig. 10.— Molecular gas depletion time, $\tau_{\rm dep} = \Sigma_{\rm H2}/\Sigma_{\rm SFR}$, as function of metallicity. The depletion times shown here correspond to the ratio of the data shown in Figure 8 including regions with CO measurements of marginal significance. The median average $\tau_{\rm dep}$ changes systematically with metallicity: for the low metallicity bin ∼0.8 Gyr, for the intermediate metallicity bin ∼1.7 Gyr, and for the high metallicity bin ∼2.4 Gyr.

dence of the molecular depletion time, $\tau_{\rm dep}$. Massive spiral galaxies with high metallicities have considerably longer (median averaged) depletion times: ∼2.4 Gyr for systems with metallicities of $12 + \log {\rm O/H} > 8.75$ and ∼1.7 Gyr for $12 + \log {\rm O/H} = 8.65 - 8.75$, while smaller galaxies with lower metallicities have systematically shorter depletion times: ∼0.8 Gyr for systems with $12 + \log {\rm O/H} < 8.65$[17]. We find a similar trend for the scaling of $\tau_{\rm dep}$ with the maximal rotation velocity, $v_{\rm flat}$, that low mass systems with $v_{\rm flat} \lesssim 140$ km s^{-1} have $\tau_{\rm dep} < 1$ Gyr. These low mass, low metallicity systems are atomic dominated ($\Sigma_{\rm HI} \gtrsim \Sigma_{\rm H2}$) for most of their radii and show up prominently in the upper left panel of Figure 8 & 9 as the data points offset to shorter depletion times. Leroy et al. (2008) and Bigiel et al. (2008) labeled these galaxies "H I–dominated" and did not consider them in their H$_2$–SFR analysis.

TABLE 3
Relation of SFR to Different Gas Phases

Gas Phase	Rank Correlation	Power Law Index
SFR(FUV+24) vs. Gas Phase		
H I		
... all data	$0.23 \pm 0.05^{\rm a}$	···
... H I–dominated	0.52 ± 0.06	···
... H$_2$–dominated	0.41 ± 0.08	···
H$_2$		
... all data	0.88 ± 0.05	$1.0 \pm 0.1^{\rm a}$
... H I–dominated	0.75 ± 0.07	1.3 ± 0.5
... H$_2$–dominated	0.91 ± 0.07	1.1 ± 0.1
H I+H$_2$		
... all data	0.90 ± 0.05	1.6 ± 0.2
... H I–dominated	0.78 ± 0.06	2.2 ± 0.6
... H$_2$–dominated	0.92 ± 0.07	1.2 ± 0.1
SFR(Hα+24) vs. Gas Phase		
H I		
... all data	$0.21 \pm 0.05^{\rm a}$	···
... H I–dominated	0.54 ± 0.06	···
... H$_2$–dominated	0.44 ± 0.08	···
H$_2$		
... all data	0.85 ± 0.05	$1.0 \pm 0.1^{\rm a}$
... H I–dominated	0.70 ± 0.07	1.5 ± 0.7
... H$_2$–dominated	0.91 ± 0.08	1.1 ± 0.1
H I+H$_2$		
... all data	0.90 ± 0.05	1.7 ± 0.2
... H I–dominated	0.79 ± 0.06	2.5 ± 0.8
... H$_2$–dominated	0.92 ± 0.08	1.3 ± 0.1

[a] Estimation of uncertainties equal to Table 2.

4.1.4. *SFR, HI, and H$_2$*

The question of which gas component — H I, H$_2$, or total gas — correlates best with recent star formation has received significant attention. Phrased this way, the question is not particularly well posed: the total gas surface density and the molecular gas fraction are closely related so that the different gas surface densities are not independent quantities. Therefore we do not necessarily expect a "best" correlation, only different functional forms. Still, it is illustrative to see how recent star formation relates to each gas tracer. Table 3 lists $r_{\rm corr}$ and the power law index from an OLS bisector fit between each component and Figure 11 shows plots for each of the three gas phases and our two SFR prescriptions. The rank correlation coefficient and the power law fits are determined for regions where we have at least a marginal CO measurement. If we restrict our analysis to high significance CO measurements, we obtain the same results within the uncertainties.

The table and figure show that recent star formation rate tracers rank–correlate approximately equally well with H$_2$ and H I+H$_2$ both across all surface densities and separately in the H I– and H$_2$–dominated regimes. H I does not correlate significantly with star formation in the H$_2$–dominated inner parts of galaxy disks, though the correlation between H I and recent star formation becomes stronger in the H I–dominated outer parts of galaxies (and further increases at even larger radii; see Bigiel et al. 2010b).

The rank correlation is a non–parametric measure of how well the relative ordering of two data sets align. A high rank correlation coefficient implies a monotonic relationship but not a fixed functional form law. For total gas, the power law index relating gas and recent star formation depends fairly strongly on the subset of data used. If we focus on the regions where $\Sigma_{\rm HI} > \Sigma_{\rm H2}$, the best–fit power law relating total gas and recent star formation (from FUV+24) has an index of 2.2 ± 0.6. Where $\Sigma_{\rm HI} < \Sigma_{\rm H2}$, the index is much shallower, 1.2 ± 0.1. By contrast, the power law relating H$_2$ to recent star formation varies less across regimes, from 1.3 ± 0.5 where $\Sigma_{\rm HI} > \Sigma_{\rm H2}$ to 1.1 ± 0.1 where $\Sigma_{\rm HI} < \Sigma_{\rm H2}$. Both of these agree within the uncertainties with the fit to all data, which has slope 1.0 ± 0.1. The slight steepening of the relation in the outer disks ($\Sigma_{\rm HI} > \Sigma_{\rm H2}$) is driven by the interplay of two effects: the rather small dynamic range in gas surface densities and an increased dispersion in SFR–to–H$_2$ ratios driven by the low mass galaxies; those have high SFR–to–H$_2$ ratios and contribute mostly to the H I–dominated subset. The qualitative picture of a

---

[17] The absolute metallicity values that we quote should not be overemphasized, but the relative ordering of galaxies is fairly secure. See Moustakas et al. (2010) for more details.

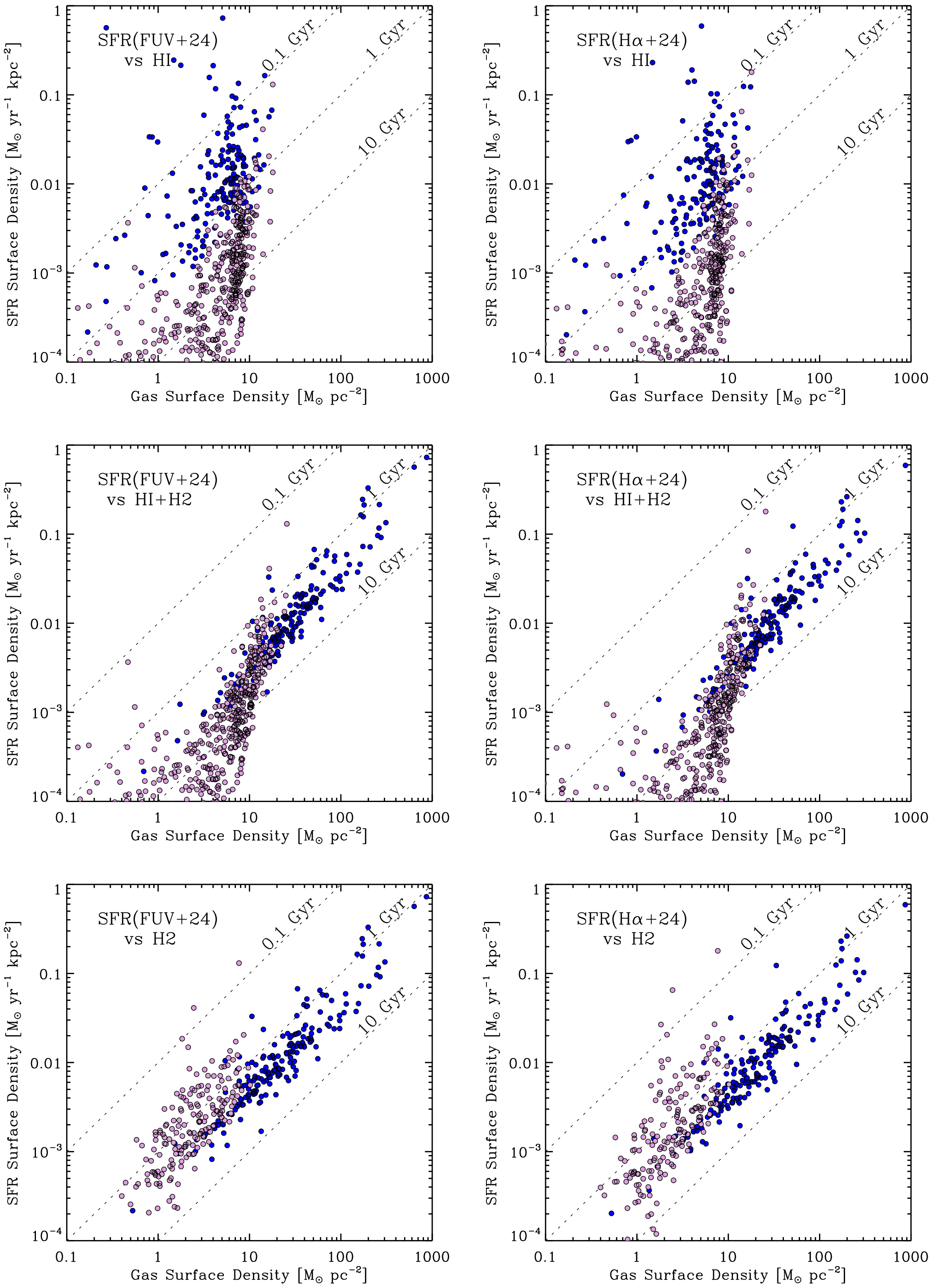

Fig. 11.— $\Sigma_{\rm SFR}$ (y–axis) from FUV+24μm (*left*) and Hα+24μm (*right*) as a function of different gas phases: H I alone (*top*), H I+H$_2$(*middle*), and H$_2$ alone (*bottom*). Each point in these diagrams represents a radial average in a given galaxy. Regions that are H$_2$–dominated are plotted with dark blue symbols, regions that are H I–dominated in light red symbols. The bottom panels show only regions with at least marginal CO signal, while the top and middle panels show also regions where we determined only an upper limit on the molecular content. Whereas SFR is not correlated to H I (in the inner parts of galaxy disks), it correlates with H$_2$ and total gas. The scaling with H$_2$ is uniform and linear for all regimes; the scaling with total gas exhibits a change in slope at the transition between H I– and H$_2$–dominated environments.

break in the total gas–SFR relation but a continuous H_2–SFR relation remains unchanged if SFR(Hα+24) is considered, though there are small changes in the exact numbers (see the left and right panels in Figure 11).

Our conclusions thus match those of Bigiel et al. (2008): a single power law appears to be sufficient to relate Σ_{H2} and Σ_{SFR} whereas the relationship between Σ_{HI+H2} and Σ_{SFR} varies systematically depending on the subset of data used. Because we have a dataset that includes significant CO measurements where $\Sigma_{HI} > \Sigma_{H2}$ we can extend these findings. First, total gas and H_2 are equally well rank–correlated with recent star formation in all regimes and this correlation is always stronger than the correlation of recent star formation with H I. Second, the H_2–SFR scaling relation extends smoothly into the regime where $\Sigma_{HI} > \Sigma_{H2}$ whereas the total gas–SFR relation does not. Third, the result is independent of our two star formation rate tracers SFR(FUV+24) and SFR(Hα+24).

4.1.5. *Discussion of CO–SFR Scaling Relations*

Empirical Results: IR brightness at both 24 μm and 70 μm correlates strongly with CO intensity over ~3 orders of magnitude. Across this range, there is a nearly fixed ratio of CO to IR emission. FUV and Hα emission show little or no correlation with CO intensity in the inner parts of galaxies, presumably due to extinction, but are found to correlate well with CO in the outer parts of galaxies after galaxy–to–galaxy scatter is removed.

A result of these empirical scaling relations is that the ratio of recent star formation rate, traced either by combining FUV and 24 μm or Hα and 24 μm intensities, to molecular gas, traced by CO emission, does not vary strongly between the H I–dominated and H_2–dominated ISM. This result is driven largely by the tight observed correlation between CO and 24 μm emission. The tight relation between CO and 70 μm emission suggests that the CO–IR relation actually holds for a larger range of mid–IR intensities. The tightening of the CO–FUV and CO–Hα relation in the outer part of galaxies (after removing galaxy–to–galaxy scatter) reinforce the idea of a linear relation extending to large radii. These tight correlations are consistent with the conclusion of Leroy et al. (2008) that there is only weak variation in the SFR per unit molecular gas mass with local environment.

Galaxy–to–Galaxy Scatter: Each of the correlations we observe has significant internal scatter. Breaking this apart into scatter among galaxies and scatter within galaxies, we observe that in every case scatter among galaxies drives the overall scatter in the observed correlation. This "scatter" among galaxies is not random; less massive, less metal–rich galaxies exhibit a higher ratio of SFR tracer to CO emission (see Figure 10 and Young et al. 1996). There are two straightforward physical interpretations for this. The efficiency of star formation from H_2 gas may be genuinely higher in these systems, a view advocated by Gardan et al. (2007) and Gratier et al. (2010). Alternatively, CO emission may be depressed relative to the true amount of H_2 mass due to changes in the dust abundance. Low mass systems often have lower metallicities and correspondingly less dust, which is required to shield CO (e.g., Maloney & Black 1988; Bolatto et al. 1999; Glover & Mac Low 2010; Wolfire et al. 2010). A precise calibration of the CO–to–H_2 conversion factor as a function of metallicity is still lacking, so it is not possible at present to robustly distinguish between these two scenarios.

After removing these galaxy–to–galaxy variations we find a series of extraordinarily tight relationships between CO and tracers of recent star formation. The most striking — and puzzling — example of this is the emergence of a tight correlation between CO and FUV emission in the outer parts of galaxies ($r > 0.5\, r_{25}$). This is puzzling because one would expect the galaxy to be mostly causally disconnected over the timescales predominantly traced by FUV emission — $20 - 30$ Myr compared to a dynamical (orbital) time of a few 100 Myr. Yet, somehow the differences between galaxies affect the CO–to–FUV ratio much more than the differences between the widely separated rings represented by our data points. Galaxy–wide variations in metallicity and dust abundance probably offer the best explanation for this. These may propagate into variations in the CO–to–H_2 conversion factor and the average dust extinction. The latter may lead to scatter in estimates of SFR and both will affect $\tau_{\rm dep}$. An alternative explanation is that external processes, which affect the whole galaxy, play a large role in setting the star formation rate on timescales traced by FUV emission.

These strong galaxy–to–galaxy variations partially explain the unexpected lack of correlation between CO emission and recent SFR observed by Kennicutt (1998). They averaged across whole galaxies and in doing so conceivably lost the strong internal relations that we observe but preserved the large galaxy–to–galaxy variations that offset internal relations. The result will be an apparent lack of correlation in galaxy–averaged data that obscures the strong internal relationship. Whether there is in fact a weaker relationship between H_2 and SFR in galaxy–integrated measurements than inside galaxies depends on whether the suggested variations in star formation efficiency are real or a product of a varying CO–to–H_2 conversion factor.

(The Lack of) A Molecular Star Formation Law: With improved sensitivity to CO emission we now clearly see nearly linear relations between CO and tracers of recent star formation rate spanning from the H_2–dominated to H I–dominated parts of galaxies. Note that the relations will likely depart from these scaling relations if regions of high surface densities ($\Sigma_{H2} > 100$ M$_\odot$ pc^{-2}) or starburst galaxies are considered (e.g., Kennicutt 1998; Daddi et al. 2010; Genzel et al. 2010). The lack of strong variations in the scaling between these two quantities in the "non–starburst regime" reinforces that molecular gas is the key prerequisite for star formation. A nearly linear correlation over this whole range can also be restated as the absence of a strong relationship between the ratio Σ_{SFR}/Σ_{H2} and Σ_{H2}. This implies that Σ_{H2} averaged over a large area is not a key environmental quantity for star formation because it does not affect the rate of star formation per unit molecular gas. Apparently the global amount of H_2 directly sets the global amount of star formation but the surface density of H_2 does not affect how quickly molecular gas is converted to stars.

By contrast, the host galaxy does appear to affect the ratio of star formation rate to at least CO intensity. This indicates important environmental variations but they are not closely linked to surface density. In this sense, Figure 8 & 9 offer a counterargument against the idea of a star formation "law" in which gas surface density alone sets the star formation rate. Instead, over the disks of normal galaxies, we see star formation governed by two processes: (a) the formation of stars in molecular gas, which varies mildly from galaxy to galaxy but appears largely fixed inside a galaxy, and (b) the conversion of H I to H_2, which does exhibit a strong dependence on environment inside a galaxy, including a strong dependence on surface density (Section 4.2). In the second part of this paper we will look at this second process by measuring variations in the H_2–H I balance as a function of gas surface density and radius.

Systematic Effects: We have interpreted the observed scaling relations in terms of a relationship between molecular gas and recent star formation rate. Leroy et al. (2008) demonstrated that azimuthally averaged profiles of the FUV+24μm combination that we use here match those of several commonly used star formation rate tracers with ~50% scatter. Here we have shown that using a combination of Hα+24μm to determine the SFR leads to indistinguishable results (see Leroy et al. 2011, in prep. for more discussion). We now discuss several systematic effects that may affect the translation from observables to inferred quantities.

The most serious worry is that the IR intensity, which drives the correlations, is acting as a tracer of dust abundance and not recent star formation. Gas and dust are observed to be well mixed in the ISM, so in the extreme, this would result in plotting gas against gas times some scaling factor (the dust–to–gas ratio). A more subtle version of the same concern is that CO emission is primarily a function of dust shielding against dissociating UV radiation. If there are large variations in the abundance of dust in the ISM then it may be likely that dust emission and CO emission emerge from the same regions because that is where CO can form and evade dissociation.

A few considerations suggest that the 24 μm and the 70 μm emission are not primarily tracing dust abundance. First, over whole galaxies, monochromatic IR emission at 24 μm and 70 μm does track the SFR (with some important variations among types of galaxy; see Calzetti et al. 2010). Second, we observe a linear correlation with CO emission and not with overall gas column, which one might expect for a dust tracer. Third, both the 24 μm and 70 μm bands are well towards the blue side of the peak of the IR SED for dust mixed with non star–forming gas (Boulanger et al. 1996) and so are not likely to be direct tracers of the dust optical depth (mass). Still, a thorough investigation of the interplay between dust abundance, IR emission, and star formation is needed to place SFR tracers involving IR emission on firmer physical footing.

A less severe worry is that using dust and FUV emission makes us sensitive to an old stellar component that might not have formed locally. Our targets are all actively star–forming systems, so old here means mainly old relative to Hα emission ($\tau \sim 4$ Myr; McKee & Williams 1997). The appropriate timescale to use when relating star formation and gas is ambiguous. When studying an individual region, it may be desirable to use a tracer with the shortest possible time sensitivity. Averaging over large parts of galaxies, one is implicitly trying to get at the equilibrium relation. Therefore a tracer with a somewhat longer timescale sensitivity may actually be desirable. The typical $20-30$ Myr timescale (Salim et al. 2007) over which most UV emission (and dust heating from B stars) occurs is well matched to current estimates for the lifetimes of giant molecular clouds (Kawamura et al. 2009). This makes for a fairly symmetric measurement — with the spatial and time scales of the two axes matched — though one is comparing recent star formation with the material of future star–forming regions.

The fact that SFRs derived from FUV+24μm and Hα+24μm are essentially indistinguishable indicates that the distinction between the time scale probed by Hα (~4 Myr) and FUV ($20-30$ Myr) is not important to this study, probably because of the large spatial scales considered by our azimuthal averages.

There may also be systematic biases in our inferred $\Sigma_{\rm H2}$. We have already discussed the dependence of $X_{\rm CO}$ on metallicity as a possible explanation for the high SFR–to–CO ratio observed in lower–mass galaxies. $X_{\rm CO}$ certainly depends on metallicity. Current best estimates imply a non–linear relationship, with $X_{\rm CO}$ sharply increasing below $12+\log_{10}{\rm O/H} \sim 8.2-8.4$ (Wolfire et al. 2010; Glover & Mac Low 2010; Leroy et al. 2011). For our range of metallicities (~$8.4-9.0$) neither the estimates of $X_{\rm CO}$ nor the metallicity measurements are accurate enough that we feel comfortable applying a correction to our data. Instead, under the assumption of a fixed SFR–to–H_2 ratio, the observed SFR–to–CO ratio can be utilized to constrain the metallicity dependence of the $X_{\rm CO}$ factor. Krumholz et al. (2011) adopt a version of this approach using literature data and show that the observed metallicity variation of the SFR–to–CO ratio is broadly consistent with $X_{\rm CO}$ predicted by Wolfire et al. (2010), though with large scatter. We therefore expect that $X_{\rm CO}$ does affect our results, creating much of the observed offset to higher SFR for low–mass galaxies. Subsequent analysis, especially comparison to *Herschel* dust maps, will reveal if there are also important second–order effects at play within galaxies.

Variations in the CO$(2\rightarrow1)$/CO$(1\rightarrow0)$ line ratio create a second potential bias in $\Sigma_{\rm H2}$. We adopt a fixed ratio of 0.7 based on comparison to literature CO$(1\rightarrow0)$ data. This is somewhat higher than the observed ratio in the inner part of the Milky Way (Fixsen et al. 1999), ~0.5, though the uncertainties on that ratio are large. More important, Fixsen et al. (1999) suggest variations in the CO line ratios between the inner and outer Milky Way and there are well–established differences between normal disk and starburst galaxies. Although not immediately apparent from a comparison of HERACLES to literature CO$(1\rightarrow0)$ data (Leroy et al. 2009), such variations could affect our derived $\Sigma_{\rm H2}$ by as much as ~50%. Rosolowsky et al. (2011, in prep.) will present a thorough investigation of how the line ratio varies with environment in HERACLES.

4.2. *Distribution of Molecular Gas*

The tight correlation between SFR tracers and CO emission across all regimes strongly reinforces the primary importance of molecular gas to star formation. In this section, we therefore examine the distribution of molecular gas in galaxies. In the outer parts of spiral

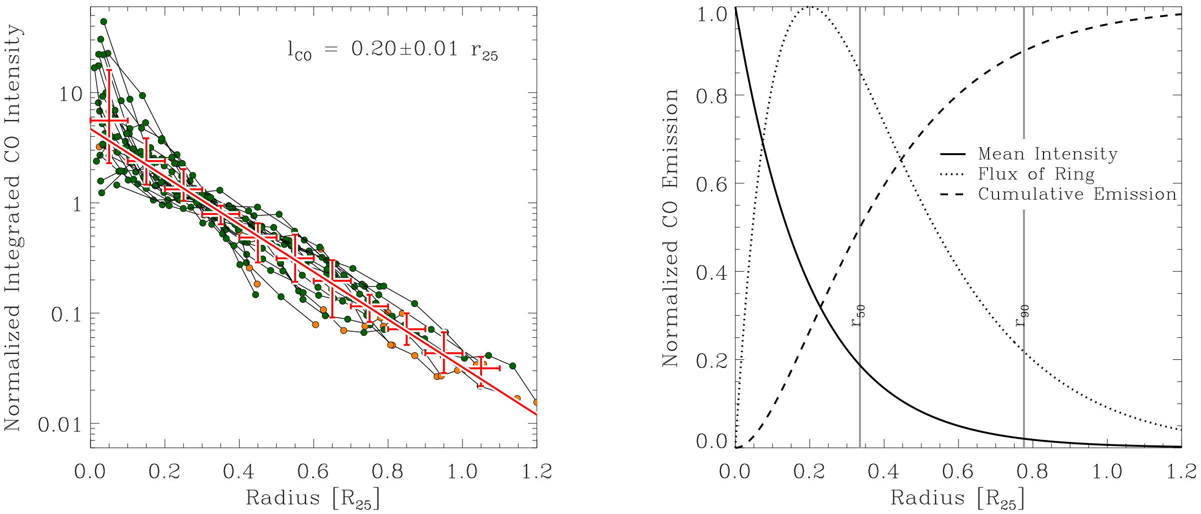

Fig. 12.— (*left*) Normalized CO intensity (y–axis) as a function of galactocentric radius (x–axis) in units of r_{25}, the 25^{th} magnitude B–band isophote for a respective galaxy. The CO intensity is normalized so that an exponential fit to the profile has intensity 1 at 0.3 r_{25}. Crosses mark the median and the 1σ scatter among galaxies in a series of radial bins (including only galaxies with at least marginal data in that bin). The average decline can be parametrized by an exponential with scale length of 0.2 r_{25} with no clear evidence of a truncation or break. (*right*) Schematic diagram for an exponential disk with scale length 0.2 r_{25}. We plot mean intensity, flux in each ring, and enclosed luminosity as functions of radius. Gray lines show r_{50} and r_{90}, the radii at which 50 and 90% of the flux are enclosed.

galaxies where $\Sigma_{\rm HI} > \Sigma_{\rm H2}$, the formation of molecular gas from atomic gas appears to represent the bottleneck to star formation and the relative abundance of H_2 and H I is key to setting the star formation rate (e.g., Leroy et al. 2008; Bigiel et al. 2010a). We can apply the large dynamic range in H_2–to–H I ratios achieved by stacking to make improved measurements of how this key quantity varies across galaxies.

4.2.1. *Radial Distribution of CO Intensity*

Many previous studies have shown that azimuthally averaged CO emission decreases with increasing galactocentric radius (e.g., Young & Scoville 1991; Young et al. 1995; Regan et al. 2001; Schuster et al. 2007). Whereas galaxy centers often exhibit deviations from the large scale trend, CO emission outside the centers declines approximately uniformly with radius (Young et al. 1995). A first analysis of the HERACLES data revealed a characteristic exponential decline of CO emission in the inner parts of galaxy disks, with the scale length of CO emission similar to that of old stars and tracers of recent star formation (Leroy et al. 2009). With the increased sensitivity from stacking and a larger sample, we can revisit this question and ask if this radial decline in CO intensity continues smoothly out to $\sim 1\ r_{25}$.

From exponential fits to the high–significance CO data of each galaxy[18] (solid–dashed lines in Figure 4 and Appendix), excluding the galaxy centers (inner $30''$) we find a median exponential scale length, $l_{\rm CO}$, of 0.21 r_{25} with 68% of all $l_{\rm CO}$ between $0.16-0.28\ r_{25}$. This value agrees well with typical scale lengths found in previous studies (e.g., Young et al. 1995) and the individual galaxy scale lengths agree well with previous work on the HERACLES sample (Leroy et al. 2009).

The normalizations of these fits reflect galaxy–to–galaxy variations in the total molecular gas content. In the left panel of Figure 12 we show all profiles aligned to a common normalization. We plot the radius in units of r_{25}, the 25^{th} magnitude B–band isophote, and normalize each profile so that the exponential fits have intensity 1 at $r_{\rm gal} = 0.3\ r_{25}$. The figure thus shows the radial variation of CO intensity across our sample, controlled for the overall CO luminosity and absolute size of each galaxy. Thick crosses mark the median CO intensity and the 68th percentile range in bins 0.1 r_{25} wide. The same exponential decline seen in individual profiles is even more evident here, with $l_{\rm CO} = 0.20 \pm 0.01\ r_{25}$ for the average of the sample.

The left panel in Figure 12 shows that the radial decline of the CO profiles observed previously for the inner part of galaxies extends without significant changes out to our last measured data points. In most galaxies there is no clear evidence for a sharp cutoff or a change in slope. As long as the normalized profiles are above the sensitivity limit the decline appears to continue (without significant deviation) with $l_{\rm CO} = 0.20\ r_{25}$ on average. This smooth exponential decline in CO intensity with increasing radius suggests that the observed decline in star formation rate from the inner to outer parts of galaxy disks is driven by a continuous decrease in the supply of molecular gas, rather than a sharp threshold of some kind.

There are several galaxies which deviate from this median exponential trend. We already noted above that we do not fit exponential profiles to NGC 2798, 2976, 4725 because their gas (H I and CO) radial profiles are insufficiently parametrized by exponentials. There are three galaxies (NGC 2146, 2903, 4569) that we do fit and determine small exponential scale lengths, $l_{\rm CO} \lesssim 0.1\ r_{25}$. NGC 2146 hosts an ongoing starburst and both NGC 2903 and NGC 4569 have prominent bars that may be funneling molecular gas to their centers. For two other

---

[18] We exclude the following galaxies from the analysis because (a) their emission is compact compared to our beam: NGC 337, 3049, 3077, 4625; (b) they are barely detected: NGC 4214, 4559; (c) their morphology is not well parametrized by an exponential: NGC 2798, 2976, 4725.

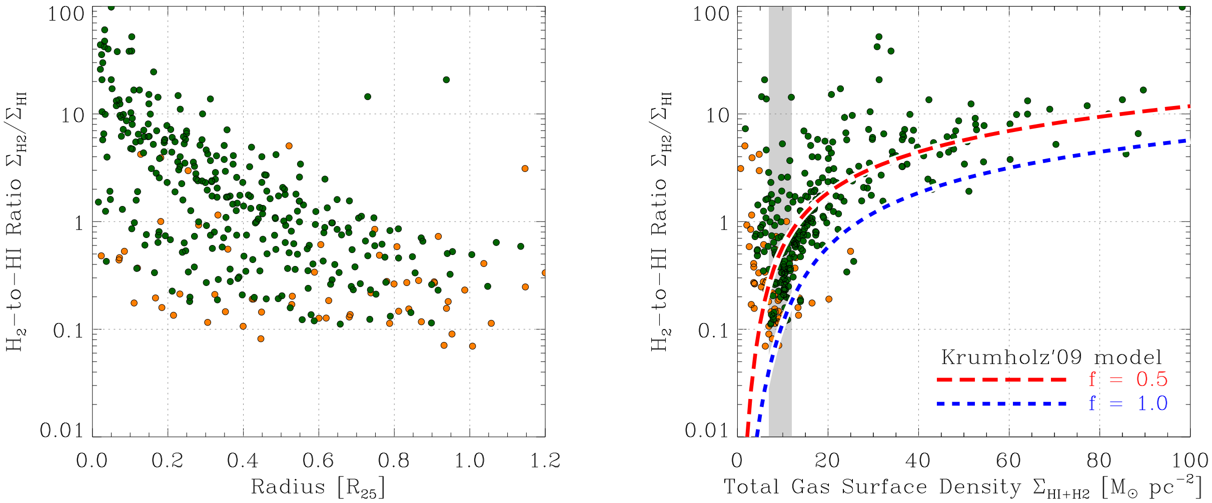

FIG. 13.— The molecular–atomic ratio, $R_{\rm H2} = \Sigma_{\rm H2}/\Sigma_{\rm HI}$ as function of galactocentric radius (left panel), and total gas surface density, $\Sigma_{\rm HI+H2}$ (right panel). The dotted line in the right panel shows $R_{\rm H2}$ as predicted by a theoretical model by Krumholz et al. (2009, see text). The gray shaded area indicates data that are shown as function of radius in Figure 14. We observe large variations in $R_{\rm H2}$ as function of radius and total gas surface density, however neither quantity is sufficient to parametrize the observed trend.

galaxies (NGC 2841 and 4579) we determine large exponential scale lengths, $l_{\rm CO} \gtrsim 0.3\ r_{25}$. These galaxies are better described by a flat distribution (or even a central depression) and a cutoff at larger radii.

The tight correspondence of the CO scale length, $l_{\rm CO}$ to r_{25} has been noted before (Young et al. 1995), while other studies have found a close correspondence between CO and near–infrared light (Regan et al. 2001; Blitz & Rosolowsky 2004). In our sample there is a fairly good correspondence between r_{25} and the near–infrared scale length, $l_{3.6}$, measured at 3.6 μm with $r_{25} \approx 4.7 \pm 0.8\ l_{3.6}$ (Leroy et al. 2008, a treatment of a larger sample suggests a slightly lower ratio of ∼4.1 with similar error bars). The near–infrared light should approximately trace the distribution of stellar mass, so that our measured scale length is very similar to that of the stellar mass. This tight coupling has been interpreted to indicate the importance of the stellar potential well to collecting star–forming material (Blitz & Rosolowsky 2006). Here we see this correspondence to continue into the regime where the molecular gas is not the dominant gas component, confirming that molecular gas formation is the bottleneck to star formation.

The right panel in Figure 12 shows the distribution of enclosed luminosity, mean intensity, and flux at each radius for an exponential disk with scale length of 0.2 r_{25}. The brightest individual ring for such a disk lies at 0.2 r_{25} and half the flux is enclosed within $r_{50} \approx 0.3\ r_{25}$. This value, r_{50}, is fairly close to the radius at which $\Sigma_{\rm HI} \approx \Sigma_{\rm H2}$ in a typical disk galaxy (see the left panel of Figure 13 and Leroy et al. 2008), so that CO emission is about evenly split between the H$_2$–dominated and H I–dominated parts of such a galaxy. Meanwhile, 90% of the flux lies within $r_{90} \sim 0.8\ r_{25}$ a value that is very similar to the threshold radius identified by Martin & Kennicutt (2001). We do not find evidence to support a true break at this radius, but as an “edge” to the star–forming disk, a 90% contour may have utility.

4.2.2. *The H$_2$–to–HI Ratio*

In the outer parts of galaxy disks — and thus over most of the area in galaxy disks — we have $\Sigma_{\rm HI} \gtrsim \Sigma_{\rm H2}$, implying that star–forming H$_2$ gas does not make up most of the interstellar medium. In this regime the relative abundance of H$_2$ and H I is a key quantity to regulate the star formation rate. Observations over the last decade have revealed strong variations of the fraction of gas in the molecular phase as a function of galactocentric radius, total gas surface density, stellar surface density, disk orbital time, and interstellar pressure (Wong & Blitz 2002; Heyer et al. 2004; Blitz & Rosolowsky 2006; Leroy et al. 2008; Wong et al. 2009). In Figure 13 we show the two most basic of these trends, the H$_2$–to–H I ratio, $R_{\rm H2} = \Sigma_{\rm H2}/\Sigma_{\rm HI}$, as a function of normalized galactocentric radius (left panel) and total gas surface density (right panel). We focus on $R_{\rm H2}$ because it is more easily separated in discrete observables than the fraction of gas that is molecular, $f_{\rm H2} = \Sigma_{\rm H2}/(\Sigma_{\rm HI} + \Sigma_{\rm H2}) = R_{\rm H2}/(1 + R_{\rm H2})$. This makes it easier to interpret uncertainties and systematic effects like changes in the CO–to–H$_2$ conversion factor.

The left panel of Figure 13 shows $R_{\rm H2}$ as function of galactocentric radius in units of r_{25} for all data detected with high or marginal significance. For clarity, we do not plot $R_{\rm H2}$ for regions where we determined only upper limits in CO intensity; for the inner parts ($r < 0.6\ r_{25}$) these upper limits are bounded by $R_{\rm H2} \lesssim 0.3$, whereas for outer parts ($r > 0.6\ r_{25}$) the upper limits in $\Sigma_{\rm H2}$ are typically of comparable magnitude as measurements of $\Sigma_{\rm HI}$ and upper limits are bounded by $R_{\rm H2} \lesssim 1$. In agreement with Wong & Blitz (2002), Heyer et al. (2004), Bigiel et al. (2008), and Leroy et al. (2008) we find $R_{\rm H2}$ to decline with increasing galactocentric radius, a variation that reflects the distinct radial profiles of atomic and molecular gas. However, radial variations alone do not explain the full range of observed molecular fractions because $R_{\rm H2}$ can vary by up to two orders of magnitude at any given galactocentric radius.

A significant part of the variations in $R_{\rm H2}$ at a given galactocentric radius corresponds to systematic variations between galaxies. These are mainly caused by variations in the absolute molecular gas content of a galaxy and can be removed by a normalization procedure similar to one applied in the left panel of Figure 12. The result is similar to that seen for the radial profiles of CO: the relationship tightens and we can see that most of the decline of $R_{\rm H2}$ inside a galaxy occurs radially. However, there is significantly more scatter remaining in $R_{\rm H2}$ versus radius than we observed for the normalized CO radial profiles, highlighting the importance of parameters other than a combination of radius and host galaxy to set $R_{\rm H2}$.

In addition to declining with increasing galactocentric radius, $R_{\rm H2}$ increases as the total gas surface density, $\Sigma_{\rm gas} = \Sigma_{\rm HI}+\Sigma_{\rm H2}$, increases. The more gas that is present along a line of sight, the larger the fraction of gas that is molecular. The right panel of Figure 13 shows this result, plotting $R_{\rm H2}$ as function of the total gas surface density, $\Sigma_{\rm gas}$. $R_{\rm H2}$ increases with increasing $\Sigma_{\rm gas}$, with regions of high surface density, $\Sigma_{\rm gas} \gtrsim 20$ M$_\odot$ pc^{-2}, being predominately molecular, $R_{\rm H2} \gtrsim 1$.

At high $\Sigma_{\rm gas}$, the right panel of Figure 13 is largely a way of visualizing the "saturation" of $\Sigma_{\rm HI}$ on large scales in galaxies. A number of authors have found that averaged over hundreds of parsecs to kpc scales, $\Sigma_{\rm HI}$ rarely exceeds $\sim$10 M$_\odot$ pc^{-2} (Wong & Blitz 2002). This limit is clearly violated at high spatial resolution (e.g. Kim et al. 1999; Stanimirovic et al. 1999; Brinks & Shane 1984) and may vary among classes of galaxies. Several recent theoretical works have aimed at reproducing this behavior. Krumholz et al. (2009) focused on shielding of H$_2$ inside individual atomic–molecular complexes, whereas Ostriker et al. (2010) examined the interplay between large–scale thermal and dynamical equilibria.

The right panel in Figure 13 includes also the predicted solar–metallicity $\Sigma_{\rm gas}$–$R_{\rm H2}$ relation from Krumholz et al. (2009, their Equations 38 & 39). They model individual atomic–molecular complexes, however these complexes have a filling factor substantially less than 1 inside our beam. The appropriate $\Sigma_{\rm gas}$ to input into their model is therefore the average surface densities of the complexes, $\Sigma_{\rm comp}$, within our beam, which will be related to our observed surface density, $\Sigma_{\rm gas}$, by the filling factor, f, namely: $\Sigma_{\rm gas} = f\ \Sigma_{\rm comp}$. The model curve (blue short–dashed line) with a filling factor $f = 1$ is offset towards higher $\Sigma_{\rm gas}$ (shifted right) or lower $R_{\rm H2}$ (shifted down) compared to our data. To have the model curve intersect our data (red long–dashed line) requires a filling factor of $f \approx 0.5 - 1$, so that atomic–molecular complexes fill about half the areas in our beam. This is before any accounting for the presence of diffuse H I not in star–forming atomic–molecular complexes and is assuming a fixed filling factor, both of which are likely oversimplifications. Nonetheless, the Krumholz et al. (2009) curve does show an overall good correspondence to our data.

As with the radius, the total gas surface density predicts some of the broad behavior of $R_{\rm H2}$ but knowing $\Sigma_{\rm gas}$ does not uniquely specify the amount of molecular gas, particularly at low $\Sigma_{\rm gas}$. This are visible as the large scatter in $R_{\rm H2}$ at low surface densities in the right panel of Figure 13. The scatter reflects a dependence of $R_{\rm H2}$ on environmental factors other than gas surface density. Figure 14 shows $R_{\rm H2}$ over the small range $\Sigma_{\rm gas} = 7 - 12$ M$_\odot$ pc^{-2}, i.e., the data from the gray highlighted region in Figure 13. We plot histograms for several radial bins which are clearly offset, indicating an additional radial dependence of $R_{\rm H2}$. At small radii ($r \lesssim 0.3\ r_{25}$) we observe a large scatter in $R_{\rm H2}$ for $\Sigma_{\rm gas} = 7 - 12$ M$_\odot$ pc^{-2} whereas at large radii ($r \gtrsim 0.6\ r_{25}$) gas with this surface density is always predominantly H I.

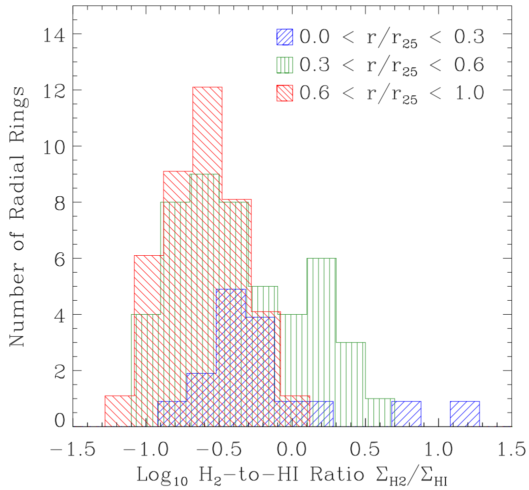

FIG. 14.— The radial dependence of $R_{\rm H2}$ for regions with comparable total gas surface density, $\Sigma_{\rm HI+H2} = 7 - 12$ M$_\odot$ pc^{-2}. The data are taken from the gray highlighted region in the left panel of Figure 13. $R_{\rm H2}$ is not sufficiently determined by the total gas surface density but shows also a radial dependence.

As was the case in SFR–H$_2$ space, distinct populations of galaxies are responsible for some of the variations in the right panel of Figure 13. Early type (Sab–Sb) spirals (e.g., NGC 2841, 3351, 3627, 4736) often show large molecular fractions, $R_{\rm H2} \gtrsim 0.5$, but typically have low H I and H$_2$ surface densities, $\Sigma_{\rm HI}$ and $\Sigma_{\rm H2} \approx 1 - 5$ M$_\odot$ pc^{-2}. By contrast, massive Sc galaxies (e.g., NGC 4254, 4321, 5194, 6946) can have comparably high molecular fractions, $R_{\rm H2} \approx 0.35 - 1$, but have higher surface density H I disks, $\Sigma_{\rm HI} \approx 5 - 10$ M$_\odot$ pc^{-2}, so that these fractions occur at higher $\Sigma_{\rm gas}$. A trend with metallicity is not immediately obvious in the data but these differences may reflect the more substantial stellar surface densities found in the earlier–type galaxies. This increased stellar surface density results in a stronger gravitational field, which could lead to a higher midplane gas pressure (Blitz & Rosolowsky 2006) and a low fraction of diffuse H I gas (Ostriker et al. 2010).

4.2.3. *Discussion of* $R_{\rm H2}$

Following several recent studies we observe strong systematic variations in the H$_2$–H I balance across galaxies. Two of the strongest behaviors are an approximately exponential decrease in $R_{\rm H2}$ with increasing galactocentric radius and a steady increase in $R_{\rm H2}$ with increasing gas surface density. Our improved sensitivity shows these trends extending to low surface densities and our expanded sample makes clear that neither of these basic parametrizations adequately captures the entire range of $R_{\rm H2}$ variations. The likely physical drivers for the scatter in $R_{\rm H2}$ that we observe are metallicity and dust–to–gas ratio (e.g., Leroy et al. 2008; Krumholz et al. 2009; Gnedin et al. 2009, Bolatto

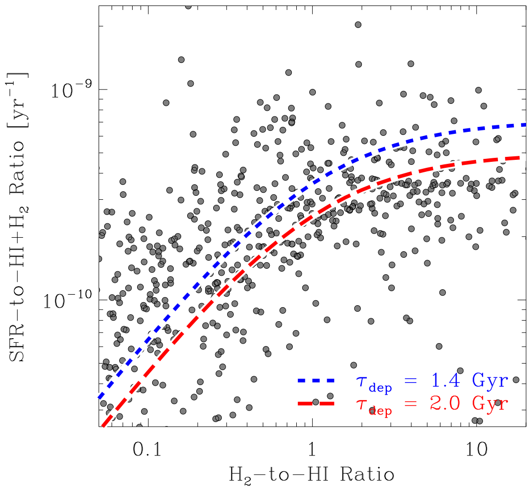

FIG. 15.— The recent star formation rate per unit total gas, $\Sigma_{SFR}/\Sigma_{HI+H2}$ (the inverse of the total gas depletion time; y–axis), as function of the molecular–atomic gas ratio, $R_{H2} = \Sigma_{H2}/\Sigma_{HI}$ (x–axis). A fixed ratio of SFR–to–H$_2$ is shown by the blue dotted line for a *molecular* gas depletion time of $\tau_{dep} \approx 1.4$ Gyr and by the red dashed line for $\tau_{dep} \approx 2$ Gyr. In regions dominated by molecular gas ($R_{H2} > 1$) the $\Sigma_{SFR}/\Sigma_{HI+H2}$ ratio approximates a value corresponding to the constant molecular depletion time, τ_{dep}. In regions of small molecular gas fraction ($R_{H2} < 1$) the $\Sigma_{SFR}/\Sigma_{HI+H2}$ ratio decreases significantly indicating that the total gas does not scale uniformly with the recent star formation rate.

et al. 2011, in prep.), the dissociating radiation field (e.g., Robertson & Kravtsov 2008), variations in interstellar gas pressure and density (e.g., Elmegreen 1994; Wong & Blitz 2002; Blitz & Rosolowsky 2006), and external perturbations that drive gas to higher densities (e.g., Blitz & Rosolowsky 2006; Bournaud et al. 2010). Each of these quantities are observationally accessible in our sample (e.g., Leroy et al. 2008) and estimates of the relative roles of each process will be presented in Leroy et al. (2011, in prep.).

The overall relationship of total gas and star formation rate (middle panels of Figure 11) can be reproduced by a roughly fixed ratio of SFR–to–H$_2$ within galaxies (Section 4.1.4) and the observed scaling of R_{H2} with Σ_{HI+H2} (Section 4.2.2). This is shown in Figure 15, where we plot the SFR per unit total gas, $\Sigma_{SFR}/\Sigma_{HI+H2}$ (the inverse of the *total* gas depletion time) as function of the molecular–to–atomic ratio, $R_{H2} = \Sigma_{H2}/\Sigma_{HI}$. At low surface densities, the R_{H2}–Σ_{HI+H2} relation regulates Σ_{SFR}, at high surface densities where almost all of the gas is molecular the SFR–H$_2$ scaling determines the observed ratio. This trend is well parametrized by a fixed SFR–to–H$_2$ ratio with a *molecular* gas depletion time of $\tau_{dep} \approx 1.4$ Gyr (blue dotted line) for all of our targets and $\tau_{dep} \approx 2$ Gyr (red dashed line) for big spirals (i.e. using the same sample as Bigiel et al. 2008; Leroy et al. 2008). The transition between these two regimes creates the curved shape seen in Figure 11 & 15. This offers more support for a modified version of the classical picture of a star formation threshold (Skillman 1987; Kennicutt 1989; Martin & Kennicutt 2001), in which dense, mostly molecular gas forms stars but the efficiency with which such (molecular) gas forms is a strong function of environment, decreasing steadily with decreasing gas surface density and increasing galactocentric radius.

5. SUMMARY

We combine HERACLES CO($2 \rightarrow 1$) data with H I velocity fields, mostly from THINGS, to make sensitive measurements of CO intensity across the disks of 33 nearby star–forming galaxies. We stack CO spectra across many lines of sight by assuming that the mean H I and CO velocities are similar, an assumption that we verify in the inner parts of galaxies. This approach allows us to detect CO out to galactocentric radii $\sim 1\ r_{25}$. Because we measure integrated CO intensities as low as 0.3 K km s^{-1} ($\sim$1 M$_\odot$ pc^{-2}, before any correction for inclination) with high significance, we are able to robustly measure CO intensities in parts of galaxies where most of the ISM is atomic.

Using this approach we compare the radially averaged intensities of FUV, Hα, IR, CO, and H I emission across galaxy disks. We find an approximately linear relation between CO intensity and monochromatic IR intensity at both 24 μm and 70 μm. For the first time, we show that these scaling relations continue smoothly from the H$_2$–dominated to H I–dominated ISM. Extinction causes FUV and Hα emission to display a more complex relationship with CO, especially in the inner parts of galaxies. In the outer parts of galaxy disks FUV and Hα emission do correlate tightly with CO emission after galaxy–to–galaxy variations are removed.

We use two calibration to estimate the recent star formation rate, FUV+24μm and Hα+24μm, which we compare to H$_2$ derived from CO. We find an approximately linear relation between Σ_{SFR} and Σ_{H2} in the range of $\Sigma_{H2} \approx 1 - 100$ M$_\odot$ pc^{-2} with no notable variation between the two SFR estimates. A number of recent studies (Bigiel et al. 2008; Leroy et al. 2008; Blanc et al. 2009; Bigiel et al. 2011) have also seen a roughly linear relationship between Σ_{SFR} and Σ_{H2} and have argued that it implies that the surface density of H$_2$ averaged over large scales does not strongly affect the efficiency with which molecular gas forms stars.

We do find evidence for variations in the SFR–to–CO ratio among galaxies. Indeed, most of the scatter in the relations between CO and SFR tracers is driven by galaxy–to–galaxy variations. These variations are not random, but show the trend observed by Young et al. (1996) that lower mass, lower metallicity galaxies have higher ratios of SFR–to–H$_2$ than massive disk galaxies. It will take further study to determine whether these are real variations in the efficiency of star formation or reflect changes in the CO–to–H$_2$ conversion factor due to lower metallicities in these systems. After removing these galaxy–to–galaxy variations the composite H$_2$–SFR relation is remarkably tight, reinforcing a close link between H$_2$ and star formation inside galaxies.

We compare the scaling between the surface densities of SFR and H I, H$_2$, and total gas (H I+H$_2$). The relationship between SFR and total gas has roughly the same rank correlation coefficient as that between SFR and H$_2$, but does not obey a single functional form. Where $\Sigma_{HI} > \Sigma_{H2}$ the relationship between Σ_{SFR} and Σ_{HI+H2} is steep whereas where $\Sigma_{HI} < \Sigma_{H2}$ the relationship is much flatter. Meanwhile, we observe a linear relationship between Σ_{H2} and Σ_{SFR} for the full range of $\Sigma_{H2} = 1 - 100$ M$_\odot$ pc^{-2}. Σ_{HI} and Σ_{SFR} are weakly correlated and exhibit a strongly nonlinear relation, except at very large radii.

The unbroken extension of the $\Sigma_{\rm SFR}$–$\Sigma_{\rm H2}$ relation into the H I–dominated regime suggests a modified version of the classical picture of a star formation threshold (Skillman 1987; Kennicutt 1989; Martin & Kennicutt 2001), in which stars form at fixed efficiency out of molecular gas, to first order independent of environment within a galaxy. The observed turn–over in the relation between SFR and *total* gas relates to the H_2–to–H I ratio which is a strong function of environment.

We therefore investigate the distribution of H_2 traced by CO using our stacked data and compare it to the H I. On large scales we observe CO to decrease exponentially with a remarkably uniform scale length of $\sim 0.2\ r_{25}$, again extending previous studies to lower surface densities. We find the normalization of this exponential decline to vary significantly among galaxies. The H_2–to–H I ratio, traced by the ratio of CO–to–H I intensities, also varies systematically across galaxies. It exhibits significant correlations with both galactocentric radius and total gas surface density and we present high–sensitivity measurements of both of these relationships. However, neither quantity is sufficient to uniquely predict the H_2–to–H I ratio on its own.

We thank the teams of SINGS, LVL, and GALEX NGS for making their outstanding data sets available. We thank Daniela Calzetti for helpful comments. We thank the anonymous referee for thoughtful comments that improved the paper. The work of AS was supported by the Deutsche Forschungsmeinschaft (DFG) Priority Program 1177. Support for AKL was provided by NASA through Hubble Fellowship grant HST-HF-51258.01-A awarded by the Space Telescope Science Institute, which is operated by the Association of Universities for Research in Astronomy, Inc., for NASA, under contract NAS 5-26555. The work of WJGbB is based upon research supported by the South African Research Chairs Initiative of the Department of Science and Technology and the National Research Foundation. This research made use of the NASA/IPAC Extragalactic Database (NED), which is operated by the JPL/Caltech, under contract with NASA, NASAs Astrophysical Data System (ADS), and the HyperLeda catalog, located on the WorldWide Web at http://www.obs.univ-lyon1.fr/hypercat/intro.html.

APPENDIX

Here we present the radial profiles of CO, H I, FUV, Hα, and IR at 24 μm and 70 μm used to generate the plots in this paper. We average the data in $15''$ wide tilted rings. For the CO data, we stack the shifted spectra over this area and determine the integrated CO intensity from fitting line profiles to the stacked spectrum. For the H I, FUV, Hα, and IR data we use two–dimensional maps of intensity (Section 3). We determine the 1σ scatter from the $68^{\rm th}$–percentile from the data inside each ring. We plot these as error bars but note the distinction from the uncertainty in the mean.

For each galaxy we present two plots: The left panel shows CO and H I both in units of observed intensities (K km s^{-1}, left–hand y–axis) and converted to mass surface densities (M$_\odot$ pc^{-2}, right–hand y–axis) of H_2 and H I. The color of the CO points indicates the significance with which we could determine the integrated CO intensities: green for high significance measurements, orange for measurements of marginal significance and red for 3σ upper limits. To have H_2 and H I on the same mass surface density scale, we multiplied the observed 21-cm line intensities by a factor of 312.5 (the ratio of Equations (1) and (2)). We also plot the star formation rate (SFR) surface density (M$_\odot$ yr^{-1} kpc^{-2}) determined from Hα+24μm and FUV+24μm. Black solid-dashed lines show our exponential fit to the radial CO profile. We fit all high significance data excluding galaxy centers, defined as the the inner $30''$, which often exhibit breaks from the overall profile (Regan et al. 2001; Helfer et al. 2003). The derived exponential scale lengths (in units of r_{25}, the radius of the 25^{th} magnitude B–Band isophote), appear in the lower left corner.

The right panel shows observed intensities (in MJy sr^{-1}) of our SFR tracers — Hα, FUV, 24 μm and 70 μm emission.

REFERENCES

Bigiel, F., et al. 2011, ApJ, 730, L13

Bigiel, F., Leroy, A., Seibert, M., Walter, F., Blitz, L., Thilker, D., & Madore, B. 2010a, ApJ, 720, L31

Bigiel, F., Leroy, A., Walter, F., Blitz, L., Brinks, E., de Blok, W. J. G., & Madore, B. 2010b, AJ, 140, 1194

Bigiel, F., Leroy, A., Walter, F., Brinks, E., de Blok, W. J. G., Madore, B., & Thornley, M. D. 2008, AJ, 136, 2846

Blanc, G. A., Heiderman, A., Gebhardt, K., Evans, N. J., & Adams, J. 2009, ApJ, 704, 842

Blitz, L., & Rosolowsky, E. 2004, ApJ, 612, L29

—. 2006, ApJ, 650, 933

Bolatto, A. D., Jackson, J. M., & Ingalls, J. G. 1999, ApJ, 513, 275

Boulanger, F., Abergel, A., Bernard, J., Burton, W. B., Desert, F., Hartmann, D., Lagache, G., & Puget, J. 1996, A&A, 312, 256

Bournaud, F., Elmegreen, B. G., Teyssier, R., Block, D. L., & Puerari, I. 2010, MNRAS, 1400

Brinks, E., & Shane, W. W. 1984, A&AS, 55, 179

Calzetti, D., et al. 2007, ApJ, 666, 870

Calzetti, D., et al. 2010, ApJ, 714, 1256

Daddi, E., et al. 2010, ApJ, 714, L118

Dale, D. A., et al. 2009, ApJ, 703, 517

Elmegreen, B. G. 1994, ApJ, 427, 384

Engelbracht, C. W., Rieke, G. H., Gordon, K. D., Smith, J.-D. T., Werner, M. W., Moustakas, J., Willmer, C. N. A. & Vanzi, L. 2008, ApJ, 678, 804

Fixsen, D. J., Bennett, C. L., & Mather, J. C. 1999, ApJ, 526, 207

Gao Y., & Solomon P. M. 2004, ApJ, 606, 271

Gardan, E., Braine, J., Schuster, K. F., Brouillet, N., & Sievers, A. 2007, A&A, 473, 91

Genzel, R., et al. 2010, MNRAS, 407, 2091

Gil de Paz, A., et al. 2007, ApJS, 173, 185

Glover, S. C. O., & Mac Low, M. 2010, MNRAS, 412, 337

Gnedin, N. Y., Tassis, K., & Kravtsov, A. V. 2009, ApJ, 697, 55

Gratier, P., et al. 2010, A&A, 522, A3

Helfer, T. T., Thornley, M. D., Regan, M. W., Wong, T., Sheth, K., Vogel, S. N., Blitz, L., & Bock, D. C.-J. 2003, ApJS, 145, 259

Heyer, M. H., Corbelli, E., Schneider, S. E., & Young, J. S. 2004, ApJ, 602, 723

Hitschfeld, M., Kramer, C., Schuster, K. F., Garcia-Burillo, S., & Stutzki, J. 2009, A&A, 495, 795

van der Hulst, J. M. 2002, ASPC, 276, 84

Kawamura, A., et al. 2009, ApJS, 184, 1

Kennicutt, Jr., R. C. 1989, ApJ, 344, 685

—. 1998, ARA&A, 36, 189

Kennicutt, Jr., R. C., et al. 2003a, PASP, 115, 928

Kennicutt, Jr., R. C., Bresolin, F., & Garnett, D. R. 2003b, ApJ, 591, 801

Kennicutt, Jr., R. C., et al. 2007, ApJ, 671, 333

Kennicutt, Jr., R. C. and Lee, J. C. and Funes, José G., S. J., Sakai, S. and Akiyama, S. 2008 ApJS, 178, 247

Kennicutt, Jr., R. C., et al. 2009, ApJ, 703, 1672

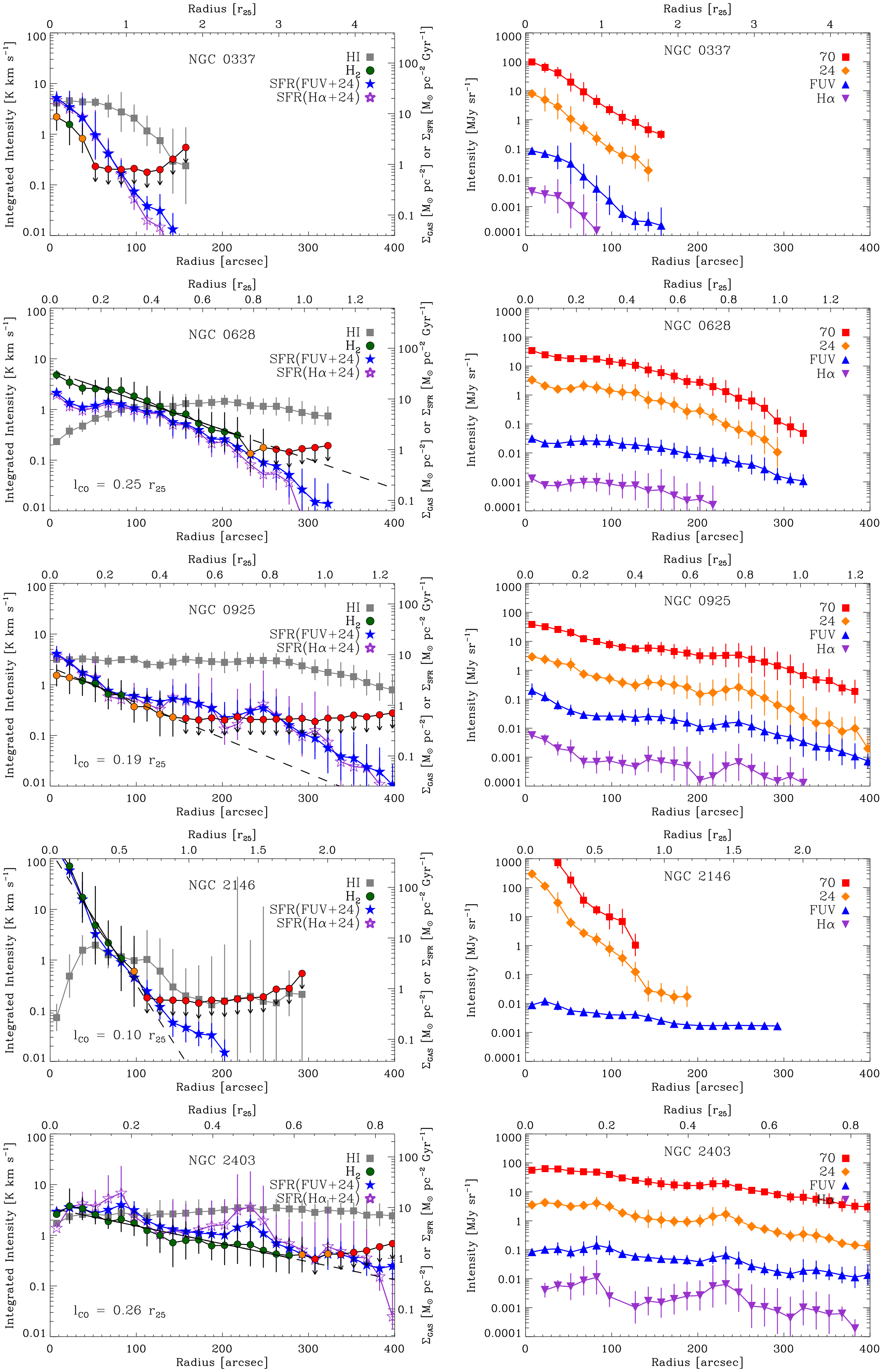

FIG. A.— Atlas of radial profiles, see Figure 4 for details.

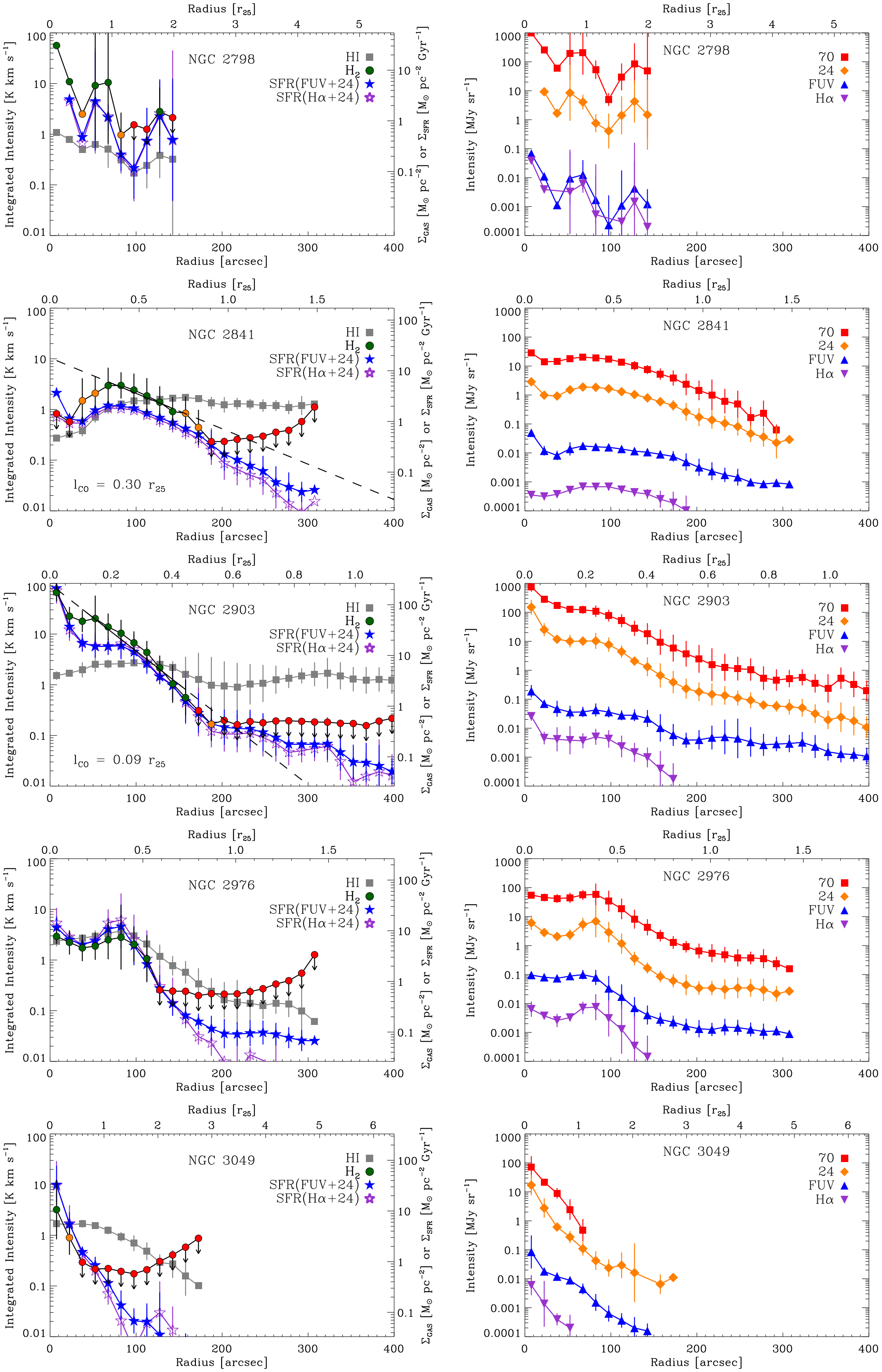

FIG. A.— Atlas of radial profiles, see Figure 4 for details.

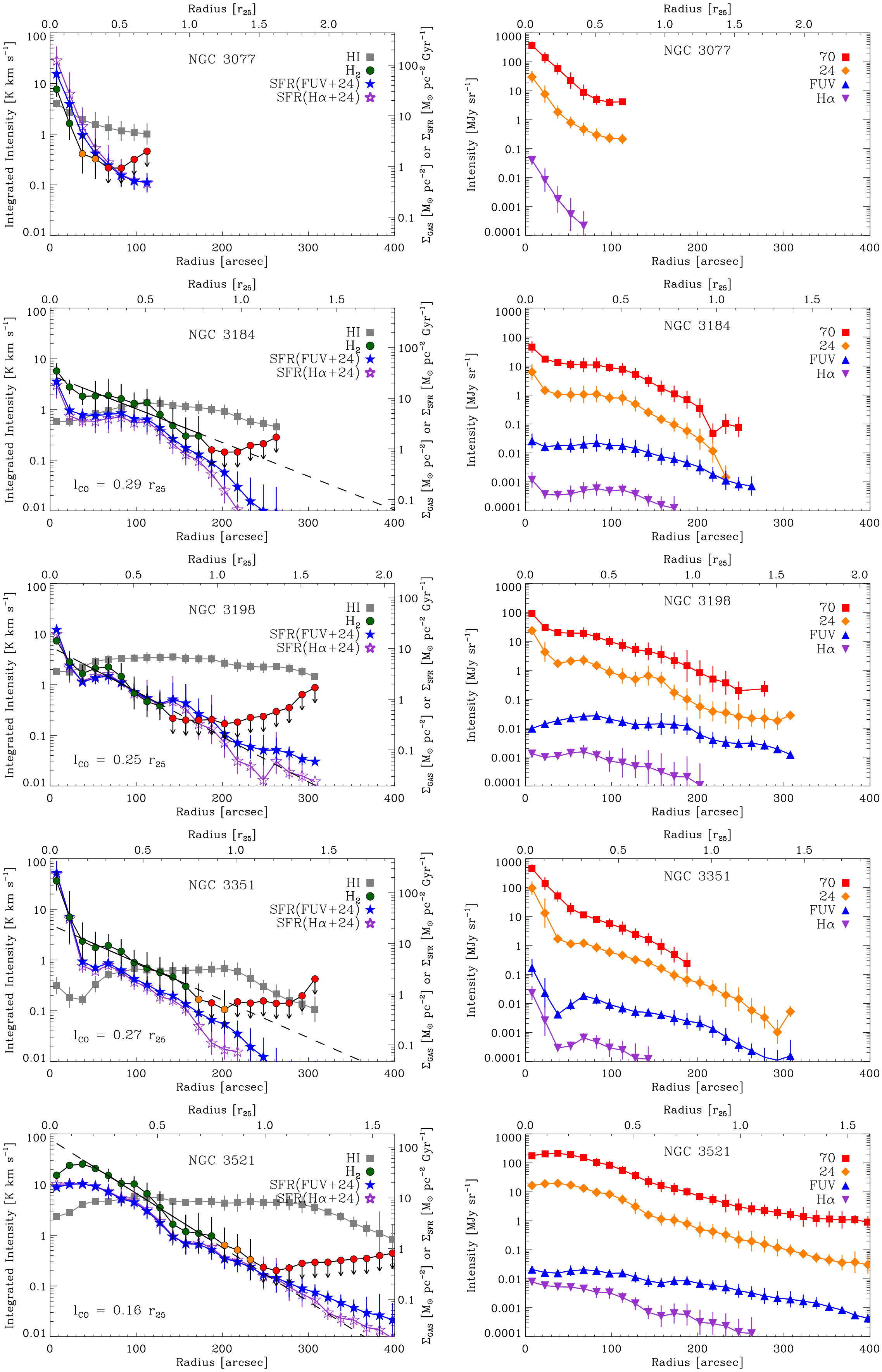

FIG. A.— Atlas of radial profiles, see Figure 4 for details.

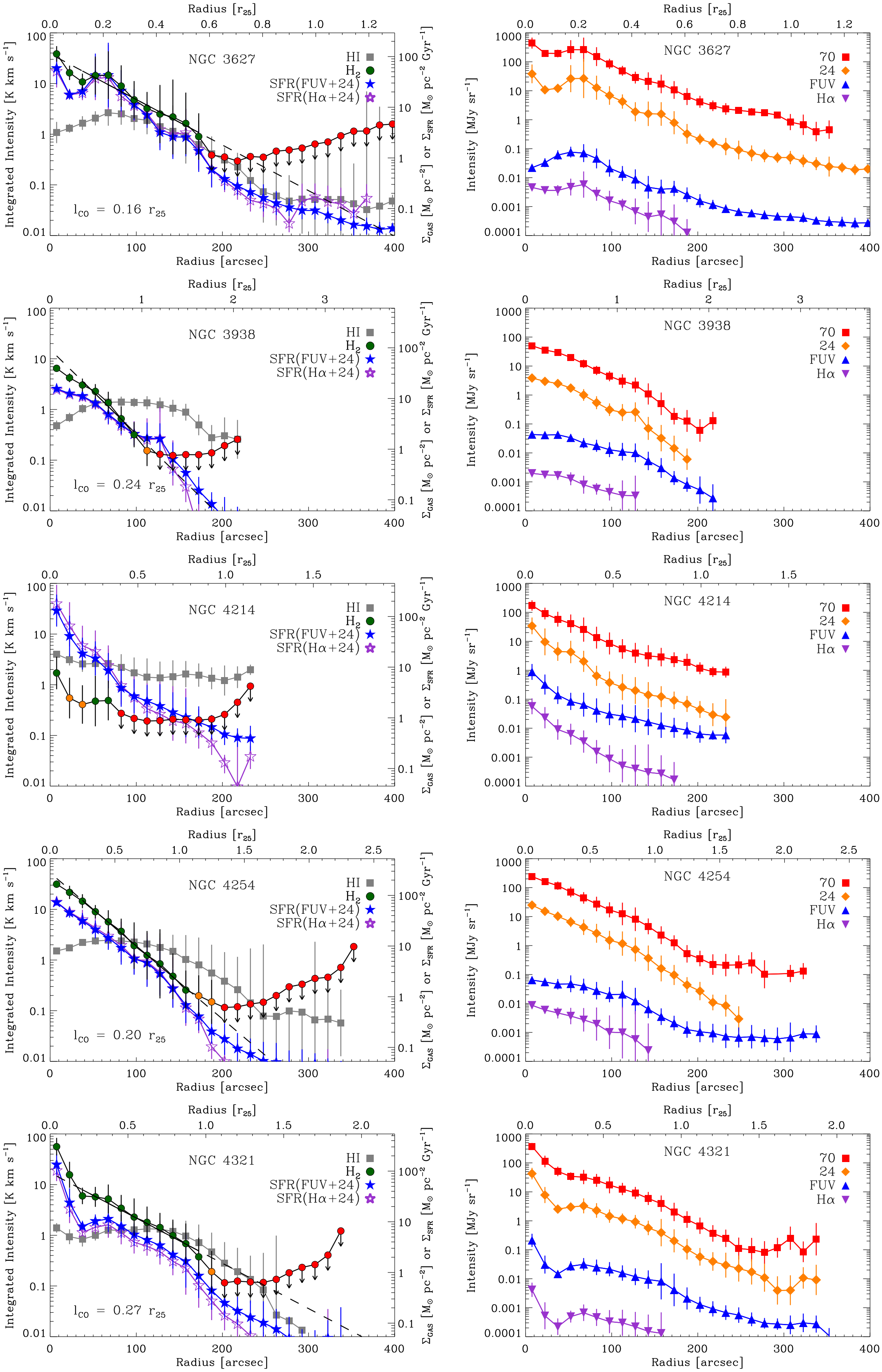

FIG. A.— Atlas of radial profiles, see Figure 4 for details.

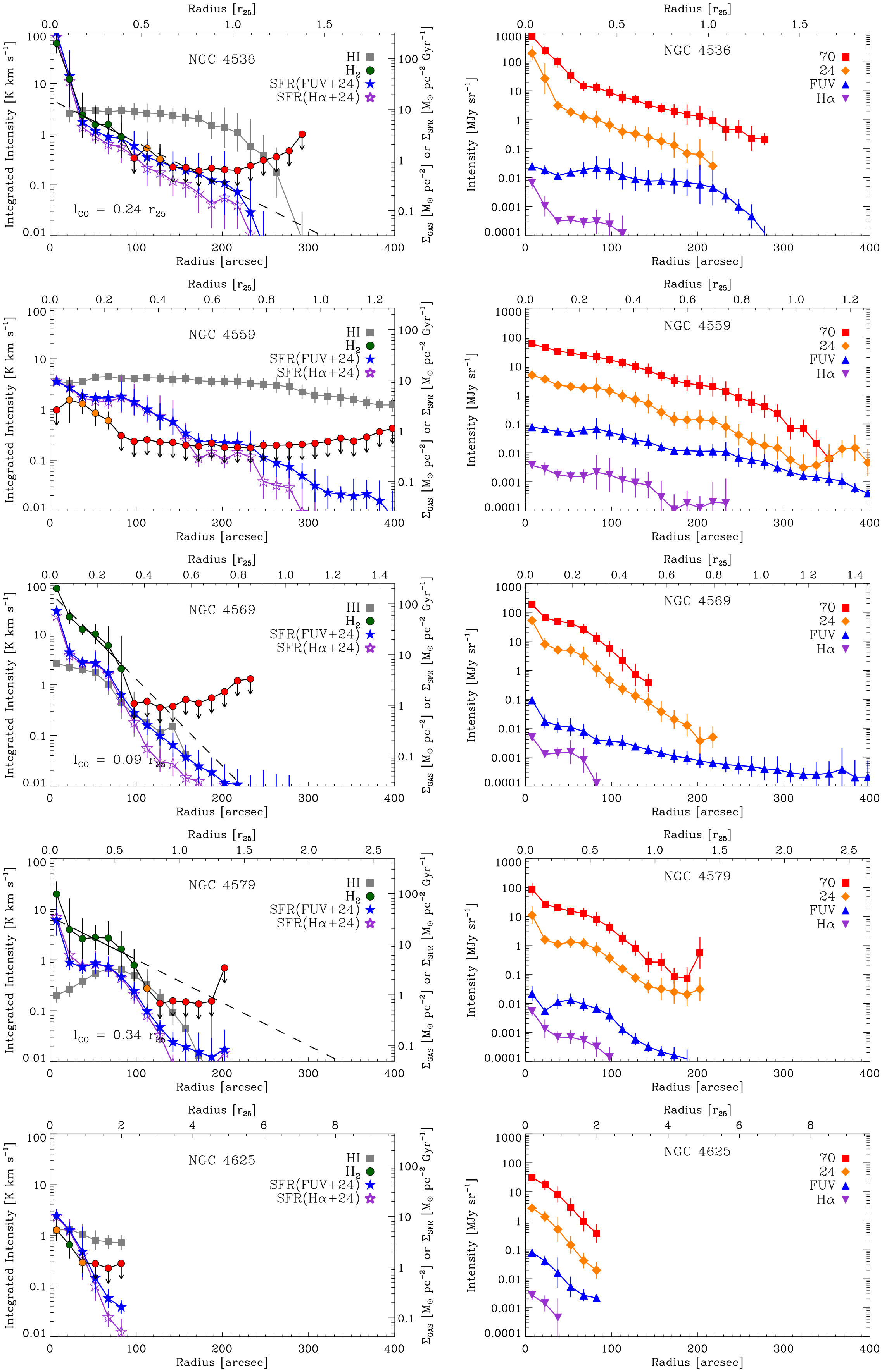

FIG. A.— Atlas of radial profiles, see Figure 4 for details.

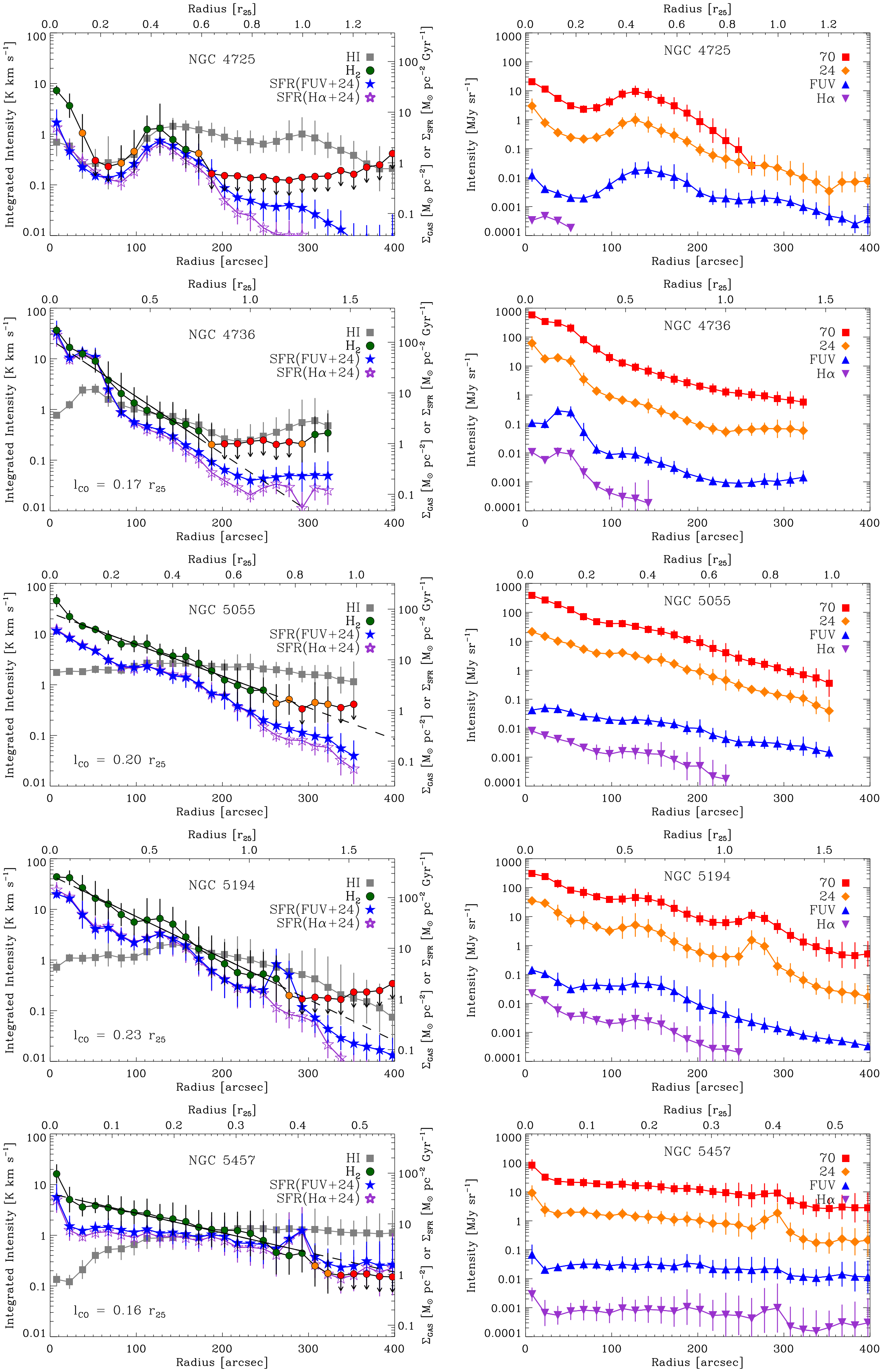

FIG. A.— Atlas of radial profiles, see Figure 4 for details.

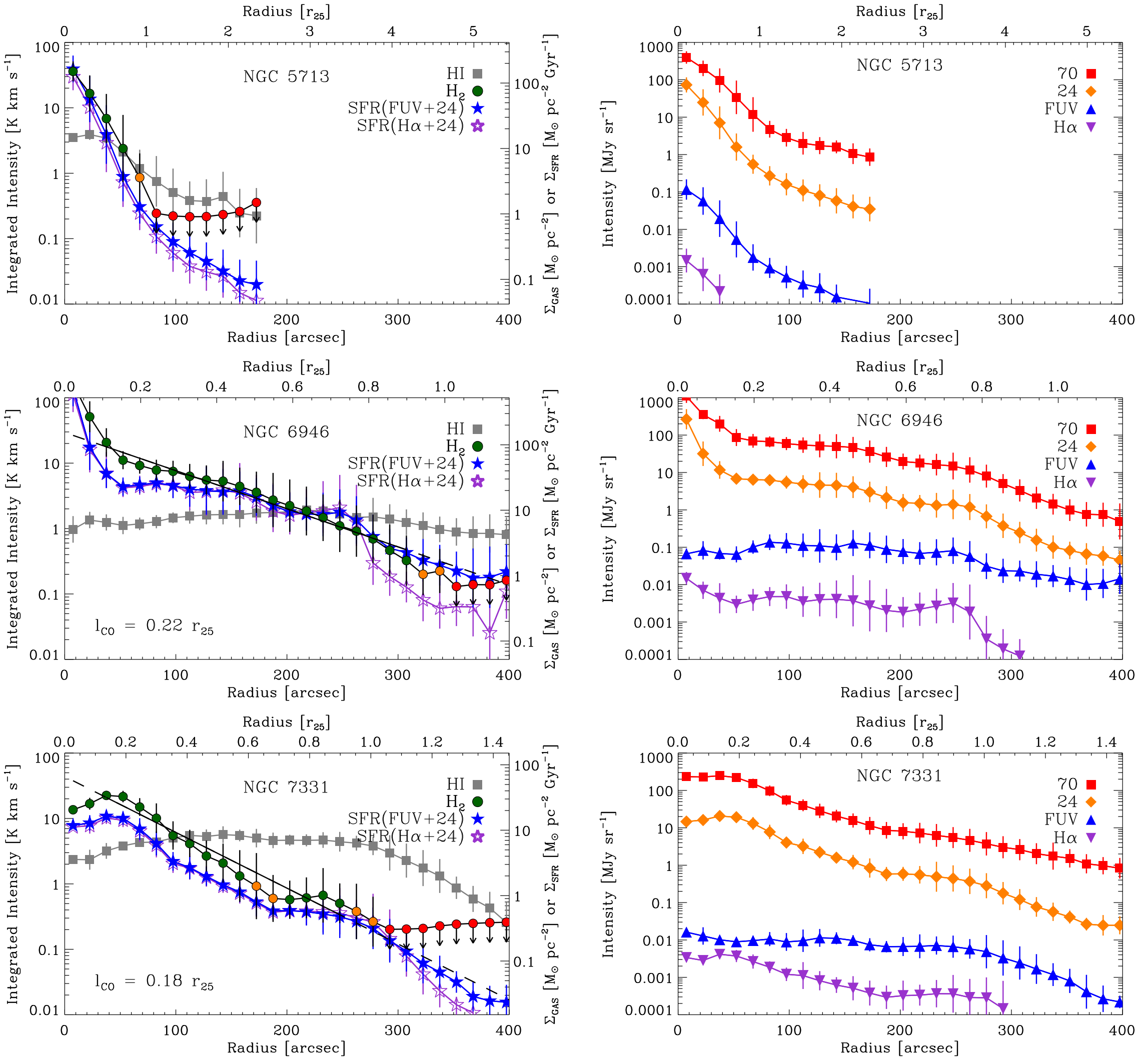

FIG. A.— Atlas of radial profiles, see Figure 4 for details.

Kim, S., Dopita, M. A., Staveley-Smith, L., & Bessell, M. S. 1999, AJ, 118, 2797

Kroupa, P. 2001, MNRAS, 322, 231

Krumholz, M. R., Leroy, A. K., McKee, C. F. 2011, ApJ, 731, 25

Krumholz, M. R., McKee, C. F., & Tumlinson, J. 2009, ApJ, 693, 216

Leroy, A. K., et al. 2011, arXiv:1102.4618

Leroy, A. K., et al. 2009, AJ, 137, 4670

Leroy, A. K., Walter, F., Brinks, E., Bigiel, F., de Blok, W. J. G., Madore, B., & Thornley, M. D. 2008, AJ, 136, 2782

Leroy, A., Bolatto, A., Walter, F., & Blitz, L. 2006, ApJ, 643, 825

Maloney, P. & Black, J. H. 1998, ApJ, 325, 389

Martin, C. L., & Kennicutt, Jr., R. C. 2001, ApJ, 555, 301

McKee, C. F., & Williams, J. P. 1997, ApJ, 476, 144

Meurer, G. R., et al. 2009, ApJ, 695, 765

Moustakas, J., Kennicutt, R. C., Jr., Tremonti, C. A., Dale, D. A., Smith, J., & Calzetti, D. 2010, ApJS, 190, 233

Muñoz-Mateos, J. C., et al. 2009, ApJ, 703, 1569

Ostriker, E. C., McKee, C. F., & Leroy, A. K. 2010, ApJ, 721, 975

Regan, M. W., Thornley, M. D., Helfer, T. T., Sheth, K., Wong, T., Vogel, S. N., Blitz, L., & Bock, D. 2001, ApJ, 561, 218

Robertson, B. E., & Kravtsov, A. V. 2008, ApJ, 680, 1083

Saintonge, A. 2007, AJ, 133, 2087

Salim, S., et al. 2007, ApJS, 173, 267

Schmidt, M. 1959, ApJ, 129, 243

Schruba, A., Leroy, A. K., Walter, F., Sandstrom, K., & Rosolowsky, E. 2010, ApJ, 722, 1699

Schuster, K. F., Kramer, C., Hitschfeld, M., Garcia-Burillo, S., & Mookerjea, B. 2007, A&A, 461, 143

Skillman, E. D. 1987, in NASA Conference Publication, Vol. 2466, NASA Conference Publication, ed. C. J. Lonsdale Persson, 263–266

Stanimirovic, S., Staveley-Smith, L., Dickey, J. M., Sault, R. J., & Snowden, S. L. 1999, MNRAS, 302, 417

Thilker, D. A., et al. 2007, ApJS, 173, 538

Vacca, W. D., Garmany, C. D., & Shull, J. M. 1996, ApJ, 460, 914

Walter, F., Brinks, E., de Blok, W. J. G., Bigiel, F., Kennicutt, R. C., Thornley, M. D., & Leroy, A. 2008, AJ, 136, 2563

Wilson, C. D., et al. 2008, ApJS, 178, 189

Wolfire, M. G., Hollenbach, D., & McKee, C. F. 2010, ApJ, 716, 1191

Wong, T., & Blitz, L. 2002, ApJ, 569, 157

Wong, T., et al. 2009, ApJ, 696, 370

Young, J. S., Allen, L., Kenney, J. D. P., Lesser, A., & Rownd, B. 1996, AJ, 112, 1903

Young, J. S., et al. 1995, ApJS, 98, 219

Young, J. S., & Scoville, N. Z. 1991, ARA&A, 29, 581